

Sensitivity and Backgrounds of Phase-I and II of the COMET Experiment

Benjamin Edward Krikler
of Imperial College London

A dissertation submitted to Imperial College London
for the degree of Doctor of Philosophy

Abstract

Declaration

This dissertation is the result of my own work, except where explicit reference is made to the work of others, and has not been submitted for another qualification to this or any other university. This dissertation does not exceed the word limit for the respective Degree Committee.

Benjamin Edward Krikler

Acknowledgements

Contents

1 Theory	2
2 The COMET Experiment	3
2.1 Overview of Signal and Backgrounds	4
2.2 General Experimental Techniques	7
2.2.1 Proton Beam Energy and Production Target	7
2.2.2 Particle Transport through Bent Solenoids	8
2.2.3 Stopping Target Material and Beam Pulsing	11
2.3 COMET Phase-I	14
2.4 COMET Phase-II	16
2.5 Schedule and Status	18
3 Offline Software and The COMET Simulation	22
3.1 Developing the COMET Offline Framework	22
3.2 Overview of ICEDUST	25
3.3 The COMET Simulation	27
3.3.1 Handling Geometry	29
3.3.2 Field Calculation	32
3.3.3 Production Target Simulations	34
3.3.4 Extending the Geant4 Physics Modelling	35
4 Phase-II Optimisation	40
4.1 Optimisation Strategy	40
4.2 Production Target Optimisation	42
4.2.1 Configuration	42
4.2.2 Length Scan	43
4.2.3 Radius scan	44
4.2.4 Final Result	45

4.3	Dipole Strengths of the Muon Beamline	48
4.3.1	Large-sample Production Target Simulation	48
4.3.2	The Optimised Dipole Field Strengths	48
4.4	Electron Spectrometer's Dipole	51
4.4.1	Method and Potential Short-comings	52
4.4.2	Results	52
4.5	Stopping Target Position	55
4.6	Collimators in the Muon Beamline	61
4.6.1	Collimator Placement	62
4.6.2	Collimator Height Optimisation	65
4.7	The Beam and Decay-in-Orbit Blockers	69
4.8	Summary of optimised parameters	72
4.9	Future optimisations	73
5	Phase-II Signal Sensitivity	71
6	Phase-II Backgrounds	72
6.1	Antiproton Induced Backgrounds	72
6.1.1	Antiproton Production Rate and Spectrum	72
6.1.2	Simulating Antiprotons	75
6.1.3	Antiproton Transmission	76
6.1.4	Delayed Pion Production	76
A	Drifts in a Bent Solenoid	78
A.1	Uniform Solenoidal Field	78
A.2	Field in a Bent Solenoid	78
A.3	Drift Calculation	79
A.3.1	Gradient Drift	79
B	Revisiting the Stopping Target Region	81
List of Acronyms		83
Bibliography		84

Chapter 1

Theory

Chapter 4

Phase-II Optimisation

The last study into the sensitivity of COMET Phase-II was performed in 2009 [14], before the staged approach and Phase-I design had even been considered. That study found that a Single-Event Sensitivity (SES) of 2.6×10^{-17} could be achieved in 2×10^7 seconds of running with a total expected background count rate of fewer than 0.34 events over the entire run period. Since then, the focus of the collaboration has shifted to the Phase-I design and R&D and the Phase-II design has not been optimised or studied further.

The purpose of this chapter is to apply the updates in the fieldmap calculation, the geometry handling and physics modelling to revisit the design of Phase-II and demonstrate that it can do at least as well as the previous 2009 design. Some aspects of the design have been fixed already by Phase-I such as the experiment hall and the coils and cold-mass of the first stages of the muon beamline. The aspects of the experiment that remain open for optimisation are shown in Table 4.1.

As an initial configuration, much of the design from the 2009 study will be used, with updates included for the areas of the experiment that have since been refined by the Phase-I design.

4.1 Optimisation Strategy

Some 32 parameters are listed in Table 4.1 and yet this number alone does not describe the full challenge of optimising the Phase-II design since many of these parameters will be correlated. It would seem natural for correlations to exist between the muon beam collimator(s), the stopping target and the beam blocker, since all involve removing or

Region for optimisation	Approx. No. of parameters
Production target dimensions and location	$3 + 3$
Torus1 dipole field strength	1
Torus2 dipole field strength	1
Muon beam collimator shapes, position, and material	$3 + 1 + 1$
Stopping target shape and location	$4 + 3$
Beam blocker position, form, and material	$3 + 3 + 1$
Electron spectrometer dipole field strength	1
DIO blockers in the spectrometer	4
Approx. total number of parameters	32

Table 4.1: The list of parameters that can be optimised and an estimate for the number of parameters that this represents. In the case of the target, beam blocker and collimator shapes the number of parameters is only approximate; crudely speaking there is at least a width, length and height but in principle one could have a very irregular shape that cannot be parametrised by only three numbers, for example shapes that change as a function of distance along the beamline.

stopping muons and other particles in the beam. Other less intuitive correlations might also exist however, and a complete optimisation would need to include the impact of these as well.

This optimisation study then can be considered a scan through a (greater than) 32 dimension parameter space. A brute force search of such a space would be nightmarishly slow and require an enormous amount of computing power. Machine learning algorithms or intelligent scanning techniques might be able to tackle such a problem, and perhaps in the future these methods will be used. In the meantime however I am forced to use the technique of 'physicists intuition' to approach the problem, whereby some parameters are assumed uncorrelated whilst others are disregarded on the expectation that their impact be small.

The goal of this chapter therefore is not only to optimise the experiment but also to evaluate the correlations. ideally this will also identify which parameters are the most strongly correlated, which would help make future optimisation studies more efficient. The outputs of this optimisation should not be considered as final but should instead be treated as a baseline from which more intelligent approaches or physicists can improve.

4.2 Production Target Optimisation

In the Phase-II Conceptual Design Report ([CDR](#)), the production target is given as being 16 cm in length and 4 mm in radius [?]. Since then, there have been changes to the magnetic field in this region, as well as the lengths and locations of solenoids, shielding and beam-pipe, and the proton beam. Previous studies have looked at comparing the Tungsten target proposed for Phase-II to other materials [?], and also drawn a comparison between MARS [?], Geant4 [?] and the limited data available.

The goal in this study then is to optimise the production target with the up-to-date configurations. This study aims to maximise the total muon and pion yield below 80 MeV at the entrance to the Torus1 bent solenoid, by varying the radius and length of the production target.

4.2.1 Configuration

Table [4.3](#) gives the key parameters for the beam input and other aspects of this simulation. The location and orientation of the target were held fixed, since the proton beamline is fixed with respect to the muon beam axis. Once a realistic proton beam becomes available, these values would also benefit from optimisation, however. During the scan over length, the back face of the target was kept 8 cm away from the muon beam since the radiation shielding has previously been optimised, and since beyond this the magnetic field will no longer be able to capture the pions and muons produced.

It must be noted that at this point in time there is an appreciable uncertainty in the proton beam profile and position. In particular, whilst the proton beamline upstream has been delivered, the effect of the magnetic field and necessary dipole and quadrupole magnetics are still being studied by the proton beam-line group. The beam profile is given in the Phase-I Technical Design Report ([TDR](#)) as having a Gaussian profile and energy distribution, but no divergence or location is given. The effect of the proton beam distribution on the overall sensitivity shall therefore be considered later on.

Protons originated from a plane (distributed as a two dimensional Gaussian across this surface) but since there is therefore some scope to tune the proton beam's position, the input particle plane was moved to remain 1 cm away from the front surface of the target. Since the aim is to maximise the muon and pion yield by varying only the length

Proton Beam

Horizontal spread, σ_x	5.8 mm
Vertical spread, σ_y	2.9 mm
Mean energy, μ_E	8.01 GeV
Energy spread, σ_E	0.135 MeV

Target

Material	Tungsten
Orientation	10° between target's principal axis and the muon beam axis.
Location	Back face fixed 8 cm away from muon beam axis.
Length	16 cm in CDR. Varied in steps of 4 cm from 4 to 32 cm.
Radius	4 mm in CDR. Varied from 2 to 10 cm in steps of 2 cm and from 10 to 30 cm in steps of 4 cm.

Software configuration

Packages	heads/1512w51_develop(3a0ee59)_3_UNCOMMITTED_
Externals	heads/Patch_Geant4-G4MultiLevelLocator(11fc8f0)
Fieldmap	160104 ((CHECK:))

Sample Sizes

Length scan	3e5 Protons on Target (POT) (30 runs of 1e4)
Radius scan	4.9e5 POT (49 runs of 1e4)
Final scan	

Table 4.2: Key parameters in the configuration of the Production Target optimisation.

and radius, shifting the proton beam input plane in this way removes any variation of target acceptance due to divergences of the proton beam in the magnetic field.

4.2.2 Length Scan

Different length targets were simulated with 3e5 POT per length. Target length was varied in steps of 4 cm from 4 to 32 cm, whilst the target radius was held fixed at the CDR value of 4 mm.

Fig. ?? shows the momentum distributions of pions and muons for different target lengths. Target length is given as half-length which is the Geant4 convention. Fig. 4.2 then shows these distributions integrated up to different momentum. From these plots it

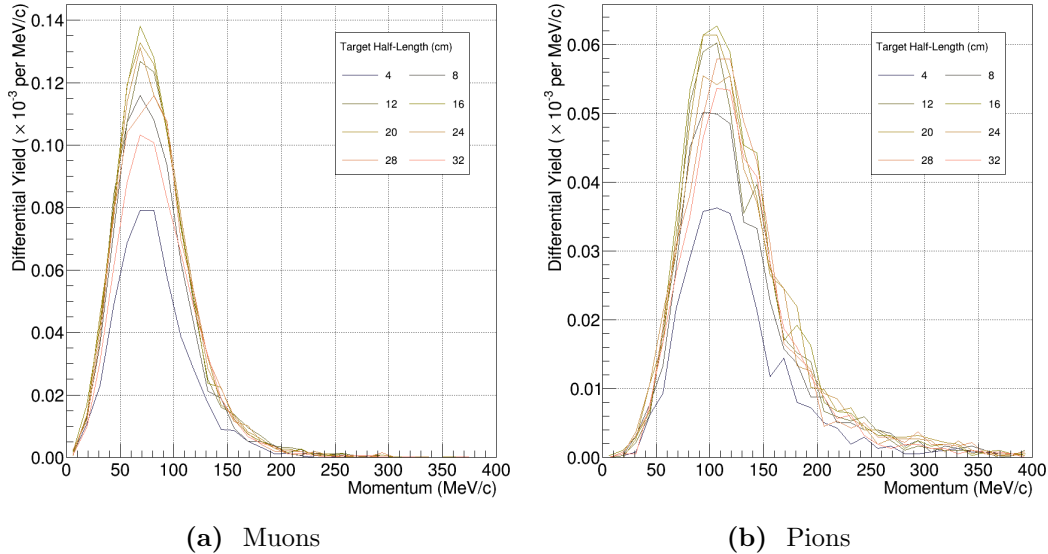


Figure 4.1: Change to momentum distributions at the entrance to the first 90 degrees of the bent muon beam solenoid for different target lengths. Target length is given as half-length which is the Geant4 convention.

can be seen that for both muons and pions, the optimum target length occurs around a total length of 32 cm.

Additionally it can be seen from Fig. 4.3 that the shape of the momentum distributions changes only weakly as a function of the target length. These plots were produced by normalising the integrated momentum contours of Fig. 4.2 to the total integral below 400 MeV. As a result, it is possible that the actual shape variation is even weaker than apparent here, since in the present sample size, the high momentum tail is not well sampled at small target lengths, such that a skew in the normalisation might occur.

4.2.3 Radius scan

In parallel to the length optimisation scan, different radii targets were also simulated. Targets with radii of 2, 4, 6, 8, 10, 14, 18, 22, 26, and 30 mm were tested. The target length was held at the CDR value of 16 cm in total.

The results of these scans can be seen in Fig. ?? and Fig. 4.5, where it can be seen that a maximum in both the muon and pion yields at the entrance to the Torus1 section is achieved at a radius of about 10 mm. As in the length scan, the shape variation of the momentum distributions is rather weak as a function of target radius.

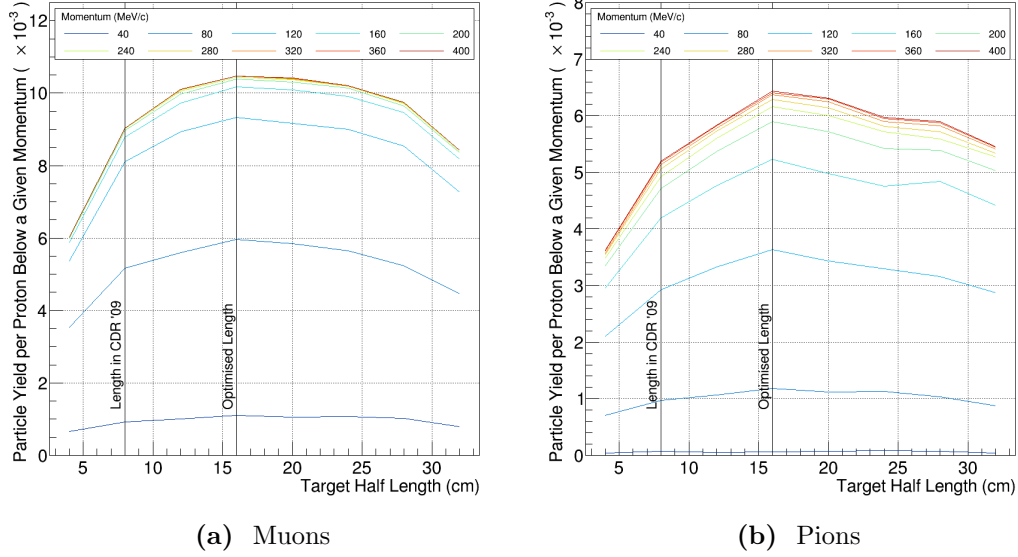


Figure 4.2: Integrated muon and pion yields up to a certain momentum at the entrance to the first 90 degrees of the bent muon beam solenoid as a function of target length.

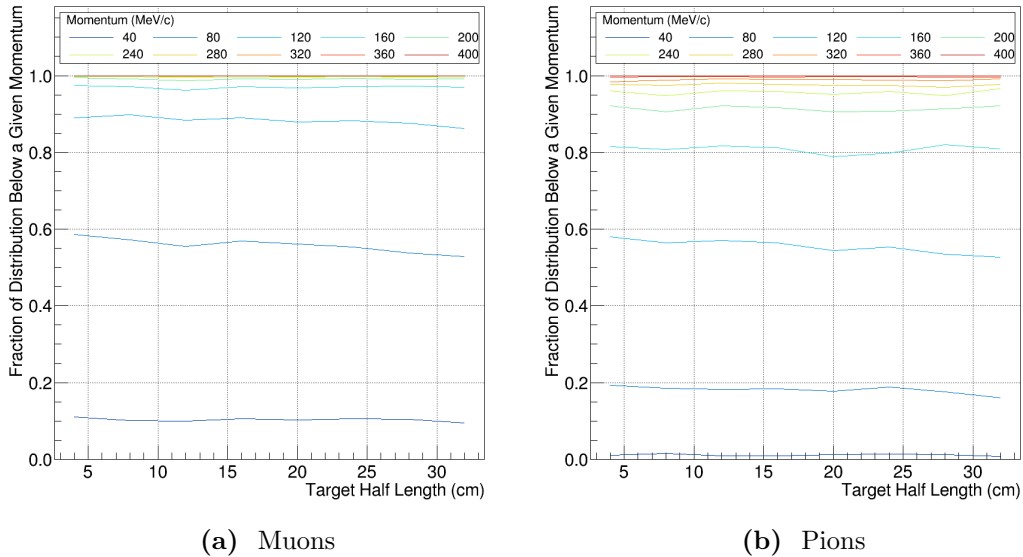


Figure 4.3: Change in the momentum distribution of muons and pions at the entrance to the first 90 degrees of the bent muon beam solenoid as a function of target length.

4.2.4 Final Result

Since the length and radius scan were performed in parallel, a final cross check was performed where the optimal radius was confirmed at the optimised target length. The

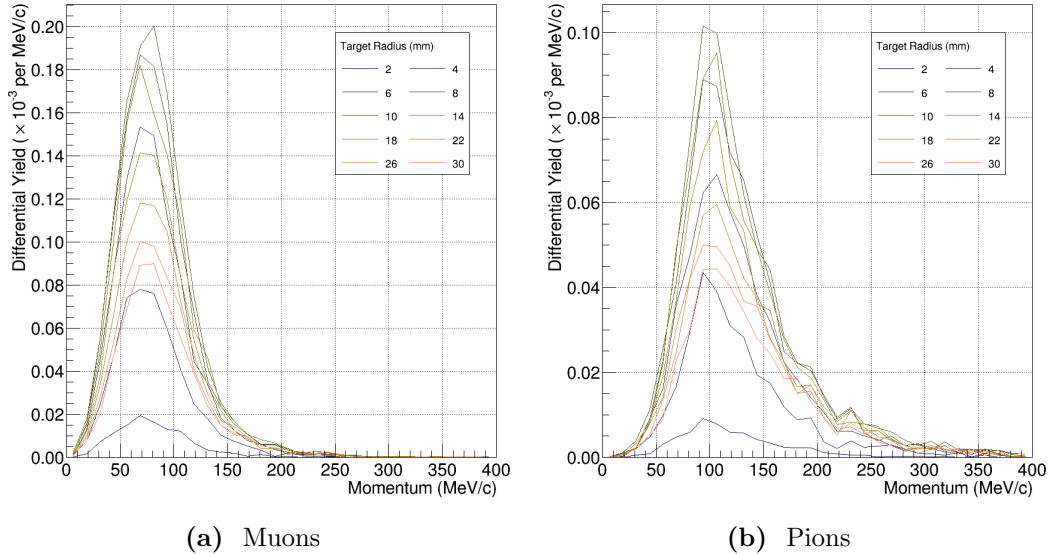


Figure 4.4: Change to momentum distributions at the entrance to the first 90 degrees of the bent muon beam solenoid for different target radii.

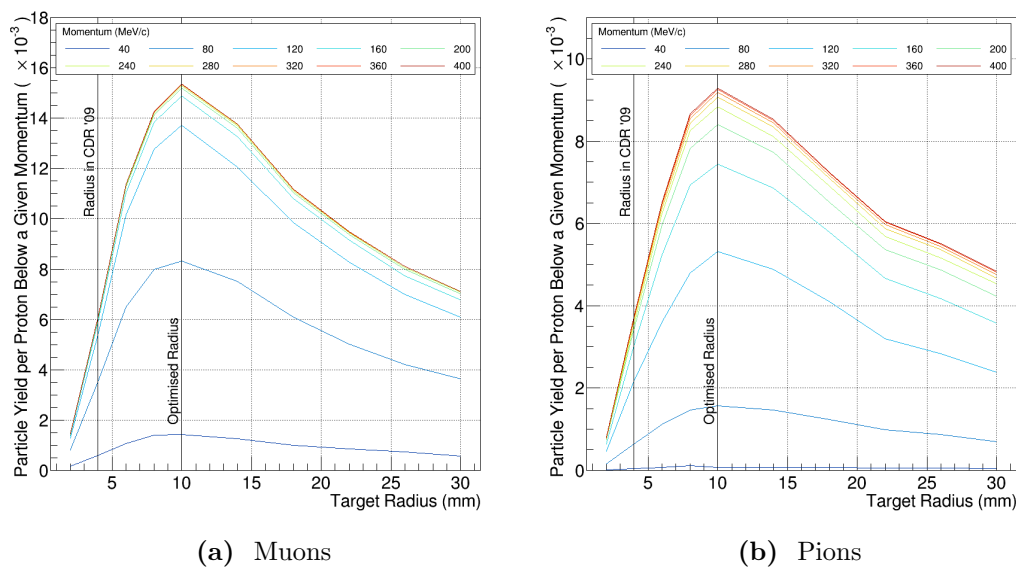


Figure 4.5: Integrated muon and pion yields up to a certain momentum at the entrance to the first 90 degrees of the bent muon beam solenoid as a function of target radius.

integrated spectrum is shown in Fig. ?? where it can be seen that the optimum radius once the target length is increased to 32 cm is still 10 mm.

- ### 1. Figure comparing Phase-II to Phase-I

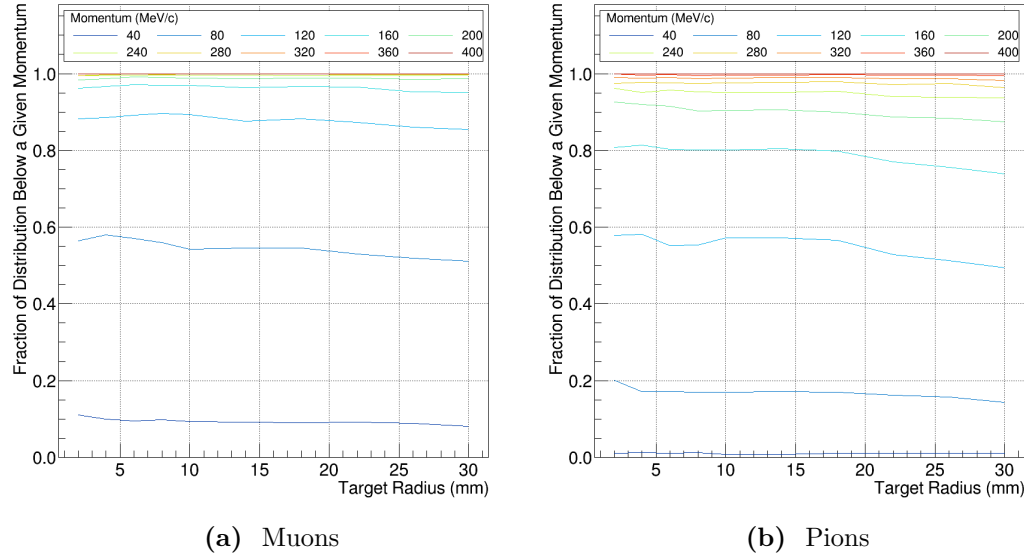


Figure 4.6: Change in the momentum distribution of muons and pions at the entrance to the first 90 degrees of the bent muon beam solenoid as a function of target radius.

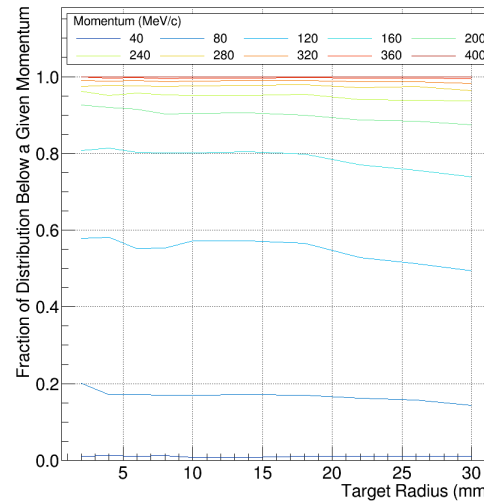


Figure 4.7: Comparison of the combined muon and pion yield at the entrance to Torus1 for Phase-I (blue) and Phase-II (red).

2. Conclusions

4.3 Dipole Strengths of the Muon Beamline

The full 180° bent solenoid that makes up the bulk of the muon transport beam line is actually broken down into two 90° pieces – Torus1 and Torus2 (also known as TS2 and TS4 by the magnet group). Each of these sections has its own dipole field which need not provide the same dipole field strength. The Torus1 section has been built already and was previously optimised for both Phase-I [28] and Phase-II [14]. The dipole coils that it contains are designed to produce a dipole field of 0.055 T. By running a lower current through these coils one could reduce the Torus1 dipole field without too much effort. However if Phase-II should require a greater dipole field strength for this region that might be trickier since it could require additional windings to be inserted – this would not be impossible but might costly.

4.3.1 Large-sample Production Target Simulation

Before the muon beam section could be optimised, a large set of POT events were produced transporting all particles up to the entrance of the muon beam section. In total, 2.4×10^8 POT were simulated through this stage, equivalent to about 1.4 bunches at Phase-II. *((CHECK: Are these numbers correct?))* The production target used the optimised geometry from the previous section. All particles that hit the surface of the Torus1 container volume were read out for later re-use. In addition, particles entering the proton beam dump were also saved if later simulations wished to study their impacts.

((CHECK: plot that shows the momentum distributions of particles in this input))

4.3.2 The Optimised Dipole Field Strengths

The figure-of-merit for this optimisation is the muon stopping rate, which will be maximised at the optimal field configuration. To identify such a configuration, a 2D-grid scan was done where the Torus1 and Torus2 dipole fields were simultaneously varied. Varying the field strength was done by applying a scale factor to the fieldmaps for each 90° section described in 3.3.2. These scale factors were varied in steps of 0.125 (equivalent to 6.875 mT) and for each point muons and pions from 8×10^6 POT were transported to

<i>((CHECK: Fill this table in properly))</i>	
Pions and muons from Prod. Tgt. simulation	
Software configuration	
Packages	---
Externals	---
Fieldmap	160104 <i>((CHECK:))</i> with additional scale factors applied to Torus dipole field
Sample Sizes	
Final scan	

Table 4.3: Key parameters in the configuration of the muon beamline dipole field optimisation.

the stopping target. The stopping rate for each combination of scale factors was then assessed.

The muon stopping rate as a function of the two dipole field strengths are shown in Fig. 4.8. A scale factor of 1 on the x-axis means no change to the current Phase-I design

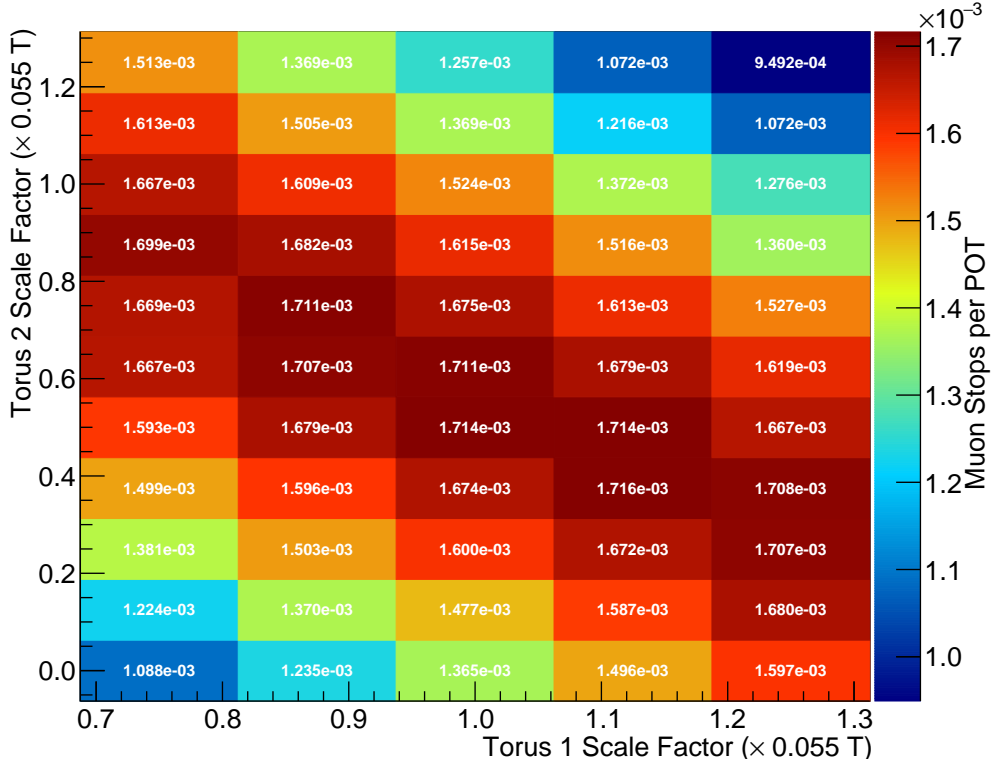


Figure 4.8: Muon stopping rate as a function of the two dipole field strengths (given relative to the Phase-I design specification). A clear anti-correlation is visible which is discussed in the text.

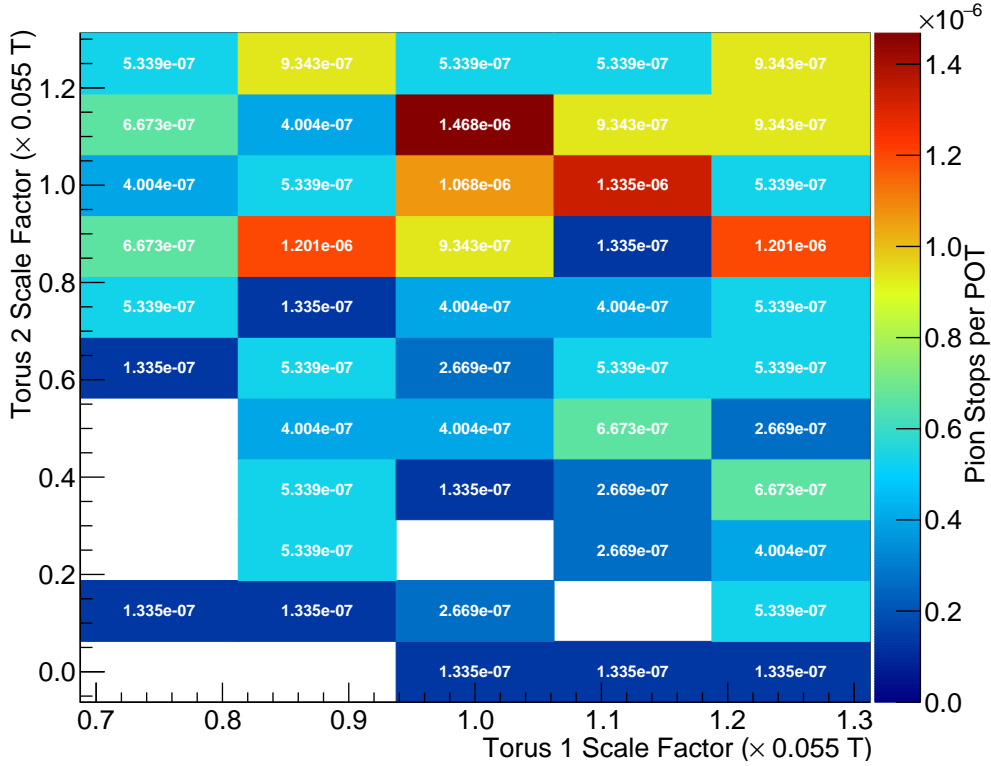


Figure 4.9: Pion stopping rate as a function of the two dipole field strengths (given relative to the Phase-I design specification). At the level of statistics used to generate each point, no clear trend is obvious. Empty squares are those where no pions stopped in the run.

and since there is little improvement by moving to larger values for Torus1 the optimal scale factors are chosen to be 1 and 0.5 for the Torus1 and TTorus2 respectively. This translates to dipole field strengths of 0.055 and 0.0275 T respectively. (*((CHECK: Are these the final selected dipole field strengths?))*)

Also striking from Fig. 4.8 is the anti-correlation between the two dipole field strengths. Roughly speaking the sum of the optimal dipole field values is constant, i.e. $B_1^{\text{optimal}} + B_2^{\text{optimal}} = \text{const}$. Although this was not previously foreseen, such a correlation can be understood accordingly. The stopping target geometry and position is held fixed in this parameter scan, which essentially fixes the upper momentum of muons that can stop in the target. The drift of a particle due to the dipole field is proportional only to the distance travelled in that dipole field and the dipole field strength, and does not depend on the particle's momentum. This means that the total drift due to the Torus1 and Torus2 dipole components is proportional to the weighted sum of the two dipole field strengths, where the weight is the distance travelled through each of the two sections. Since each section is the same length, the time for a particle to pass through Torus1

will be roughly the same as the time in Torus2 so that the weights would be roughly equal. This leads to the total drift being proportional to the sum of the two dipole fields. Since the production target (as the source of muons) and stopping target (as the muons' destination) are at a fixed height with respect to one another the optimal vertical drift is also fixed so that the sum of the dipole field strengths should also be roughly fixed.

With that said, the Torus1 section has a higher pion flux which causes some assymetry between the two sections. Keeping more pions on-axis in the Torus1 section means that more muons will enter the Torus2 section from those pions that have decayed. But since the pion momentum distribution is slightly higher than the muon distribution keeping pions on axis requires a larger dipole field strength. This could explain the slight assymetry where the muon stopping rate appears slightly larger if Torus1's field is larger than that of Torus2.

It is also interesting to consider the pion stopping rate as a function of the dipole field strengths. However, as can been from Fig. 4.9 the stopping rate is close to the level of POT events used in the simulation so that the plot is dominated by statistical fluctuations.

4.4 Electron Spectrometer's Dipole

The next element in the beamline after the muon transport solenoids will be the stopping target. However, in order to study the impact of changing the stopping target parameters one will need to look at the impact on the signal acceptance into the detector. To study that requires the components of the beamline intermediate to the target and the detector be optimised, namely the electron spectrometer. The key free parameter in this section is the dipole field strength along the spectrometer. The solenoidal field and solenoid aperture could also be optimised in principle, but these are considered beyond the scope of this study at this point and so the CDR values are held fixed here. The point of this section is to establish the optimal dipole field strength given fixed target parameters which will then be studied separately together with the stability of the dipole field tune checked.

4.4.1 Method and Potential Short-comings

To study the effect of the dipole field on signal acceptance, a realistic muon stopping distribution in the target was produced by transporting muons from the production target simulation through to the stopping target. Signal electrons were then injected at the target with the realistic stopping distribution and propagated through the beamline to the detector with different dipole field strengths.

A non-trivial short-coming of the current study is that the dipole field along the spectrometer is poorly modelled – no realistic coil simulation exists, unlike for the bent muon transport beamlines. As a result, a perfectly uniform dipole field is assumed with a sharp switch on and off at the entrance and exit of the spectrometer. The impact that this has on the final result is not clear: one might expect it to be small given the relative strengths of the dipole and solenoidal fields and overall it is the integrated field that tends to matter. However, the sharp switch-on of the field at the entrance and exit of the spectrometer is clearly not physical. Given that the gradient introduced in the field by bending is present before the actual entrance and exit of the spectrometer (as a fringe field), some drift can be anticipated in this region. A realistic dipole field with a realistic fringe field might overcome some of this drift however, so that the uniform field used here will most likely not capture this effect. Nevertheless, given the absence of a realistic dipole field and scope of this study, the uniform one is the only real option at this point.

4.4.2 Results

Fig. 4.10 shows the projection of electron trajectories to the beam axis coordinate system for three different dipole field values. The potency of this approach is clear from these plots; the tuneable dipole fields allow the momentum of electrons which remain on-axis to be accurately controlled (during run-time), which will benefit systematic and calibration studies that wish to study the decay in orbit (DIO) spectrum at a lower energy. Fig. 4.11 then collects these plots with other dipole field strengths, plotting the mean height for all simulated electrons against the distance along the beam axis. From this plot it can be seen how a dipole field of about 0.18 T appears optimal to keep the signal electrons on axis.

The probability for electrons to reach a given point in the beamline is shown in Fig. 4.12, and indeed from this it can be seen that to maximize the probability of an electron reaching the detector a dipole of around 0.18 T is desirable. The behaviour of

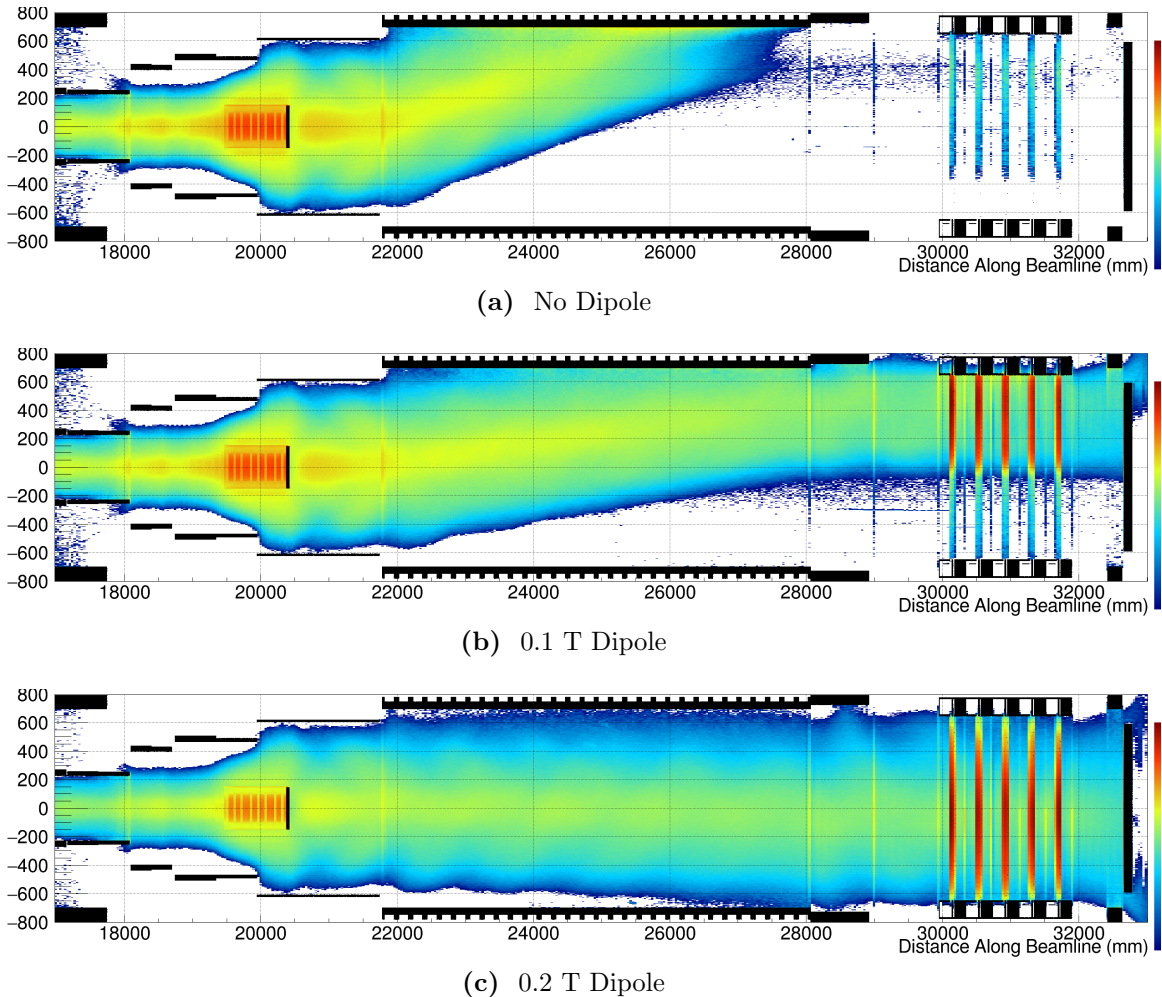


Figure 4.10: The heights of signal electrons for different dipole field values.

the low dipole field values (0 to 0.08 T) in this plot was not expected, but it is believed this is an artifact of the way this plot is made, coupled with a degree of mirroring at the entrance to the spectrometer which is enhanced as the dipole field strength increases. If correct, a realistic dipole field calculation would be important to quantify and confirm this behaviour.

Finally, to confirm the optimal dipole field strength the true geometric acceptance of the detector system is checked as a function of the dipole field strength, which is shown in Fig. 4.13. An electron is considered to have been geometrically accepted by the detector in this simulation if it produces at least one hit in the detector system. In principle this could be in any straw plane, but in practice this is almost always in the first layer of straws. Since this is a different way to analyze the acceptance compared to the survival probability it would not suffer to the artifact seen for low dipole field values in Fig. 4.12.

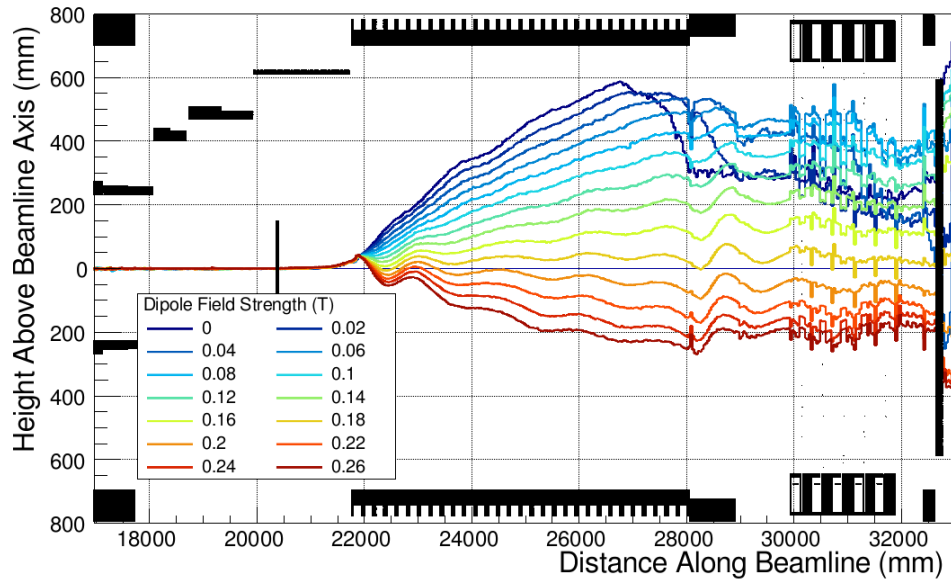


Figure 4.11: Mean height of signal electrons for different values of the dipole field strength.

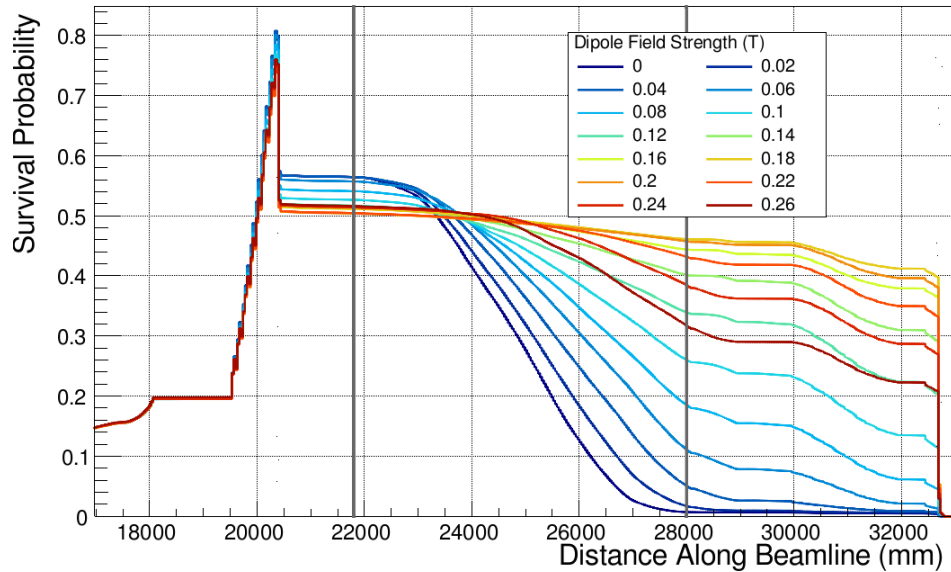


Figure 4.12: Survival probability for signal electrons as a function of the distance along the beamline for different values of the electron spectrometer's dipole field strengths.

Nonetheless, Fig. 4.13 confirms that the optimal dipole field strength is very close to 0.18 T.

A second important conclusion can be drawn from the fact that the dependence on the dipole field strength is relatively weak around the optimal value of 0.18 T. A change of about 10% in the dipole field strength only reduces the signal acceptance by about 3% whilst a change of about 5% would see a reduction of only about 0.7%.

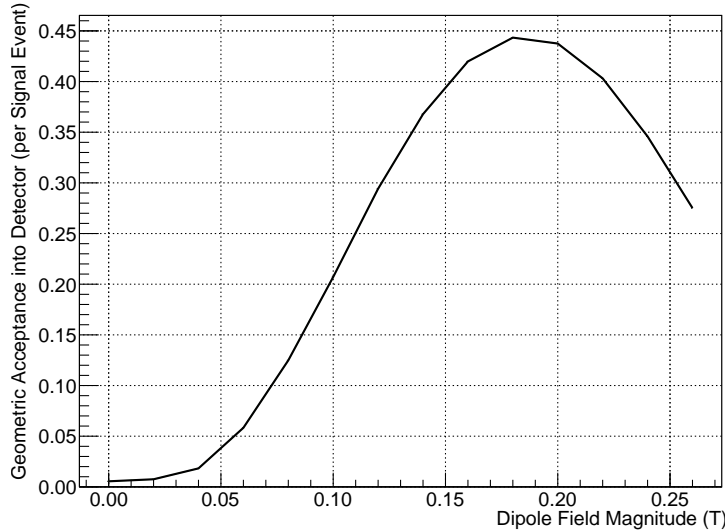


Figure 4.13: Geometric acceptance into the StrECAL detector as a function of the dipole field strength over the electron spectrometer.

4.5 Stopping Target Position

The final aspect to be studied with regards to maximizing the signal sensitivity is the stopping target. In principle there are many parameters related to the stopping target such as the location, disk shape (profile and thickness), and disk spacing. In addition the beam blocker should be considered in parallel with the stopping target since it sits so close to the target itself and can be expected to have a big impact on the signal acceptance. However, this leaves far too many parameters to be considered all at once.

Since the field around the target tapers sharply various competing factors must be considered. For example, prior to the stopping target region the muon beam is transported through a 3 T solenoidal field. The magnetic field in the target region, however, tapers to about 1 T, which would cause the envelope of the muon beam to grow. Moving the stopping target downstream would mean that the muon beam arrives with a larger aperture, and would therefore prefer a larger stopping target or else fewer muons will actually hit the target. On the other hand, from the perspective of signal acceptance, the tapered field can be used to mirror signal electrons that are initially produced heading upstream therefore increasing the signal acceptance. Moving the target further upstream then will reduce this effect as the difference between the magnetic field strengths at the exit of the bent muon transport solenoid and at the stopping target is reduced.

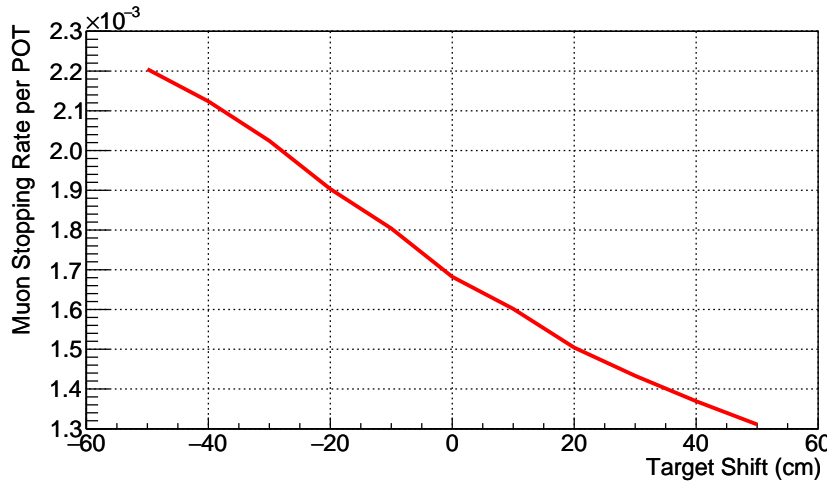


Figure 4.14: Muon stopping rate per POT for different target positions. The linear behaviour arises from the reduced field strength and fixed target radius such that fewer muons impact the target as it is moved downstream.

Given this and the need to reduce the number of parameters inspected, the target and beam blocker design was held fixed in this study and only the position was changed by moving the target upstream and downstream by ± 50 cm with respect to the nominal target location as given in the CDR [14]. Given that the target disks will occupy in total about 1 m, a shift of 50 cm corresponds to half the target length. In each different position of the stopping target, as for the spectrometer dipole optimisation, a realistic stopping distribution was produced by running muons from the large-scale production target simulation through to the target. This stopping distribution was then re-used to introduce signal electrons accordingly. Additionally, low momentum electrons were also studied in order to study the impact of target position on the height of both signal and low-energy electrons as they pass through the spectrometer. This is important both to check the correlation of the dipole field tune with the stopping target position, but also how the subsequent DIO blocker height optimisation will correlate the target position.

Fig. 4.14 shows how the rate of muon stops per POT is affected by changing the position of the stopping target. The relationship is roughly linear, dropping from around 2.2×10^{-3} muon stops per POT when the target is shifted upstream by 50 cm to about 1.3×10^{-3} muon stops per POT if the target is shifted 50 cm in the other direction. This relationship is as expected given the fixed radius of the target and the growth of the muon beam aperture arising from the reduction in the field strength.

In Fig. 4.15 one can see the way the electron acceptance changes for different target positions. Acceptance here is defined as producing at least one hit in the detector and

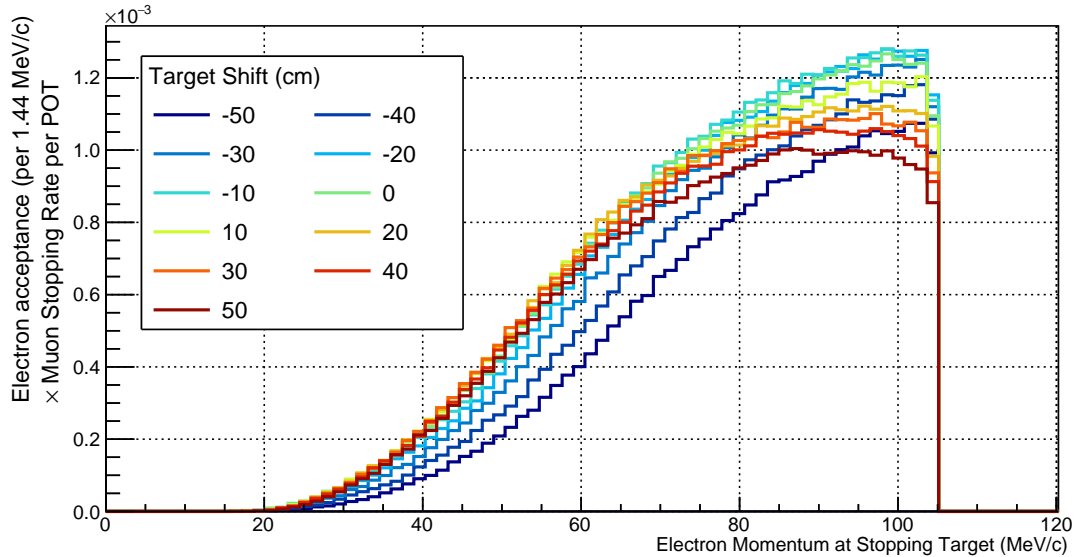


Figure 4.15: The momentum dependence of the electron acceptance into the detector for different target positions. The spectrum for each target position is normalised to the muon stopping rate for that position, such that each The linear behaviour arises from the reduced field strength and fixed target radius such that fewer muons impact the target as it is moved downstream.

the momentum shown is the momentum at the target, which is not necessarily the same as the momentum at which the electron is observed. Each histogram in Fig. 4.15 is normalised to the number of primary electrons introduced at the target per MeV/c and then scaled to the muon stopping rate. This normalisation makes the value of each curve proportional to the sensitivity of the experiment to different momentum electrons, up to factors such as analysis cuts like timing and reconstruction quality.

Since the parameter we wish to optimise here is the location of the stopping target, Fig. 4.16a represents the same data as in Fig. 4.15 but with each line representing the content of a different $5 \text{ MeV}/\text{c}$ bin as a function of the target position. For signal, it is the $105 \text{ MeV}/\text{c}$ line (dark burgundy) that is most important and it can be seen that this is optimised for shifts upstream of the nominal position from between 10 and 20 cm. It is also interesting to note that the acceptance of lower energy electrons is relatively decreased as the target is moved upstream, as can be seen in Fig. 4.16b. This could be useful as a way to suppress hit rate from DIO electrons later.

Whilst we do not intend to optimise the beam blocker at this point, to check the impact that it has on the optimisation of the target position simulations were performed where the blocker was completely removed. Fig. 4.17 shows the product of the stopping rate and electron acceptance when the blocker is removed. From this the trend is much

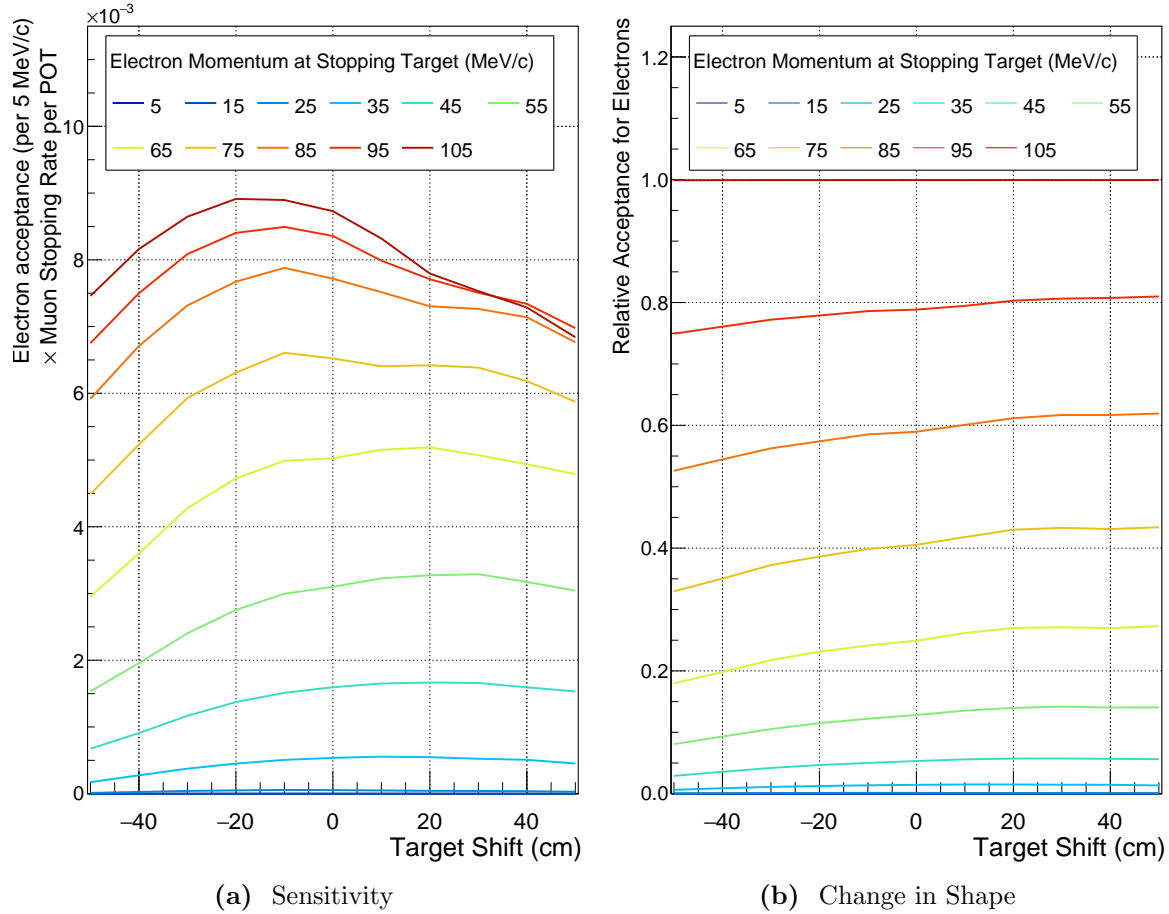


Figure 4.16: (a) The variation in sensitivity (acceptance \times stopping rate) to electrons with different momenta as a function of the target position with respect to the nominal location. The darkest red line towards the top of the plot represents the sensitivity to signal, and it is that line that should therefore be maximised. (b) The change in the shape of the acceptance vs. momentum spectrum as a function of the stopping target location.

cleaner, electrons below 70 MeV/c are suppressed as you move the target upstream whereas the high energy electron acceptance increased.

Finally the relationship between the stopping target position and the mean height of electrons through the spectrometer is demonstrated in Fig. 4.18. Each plot shows the mean heights for electrons with a given momentum for different stopping target positions and it is clear that there is some correlation between the mean height and the position of the stopping target. For this reason, a more complete optimisation should consider optimising the two parameters simultaneously. Nonetheless the change is not particularly large, only about a few cm difference by the end of the spectrometer for signal electrons.

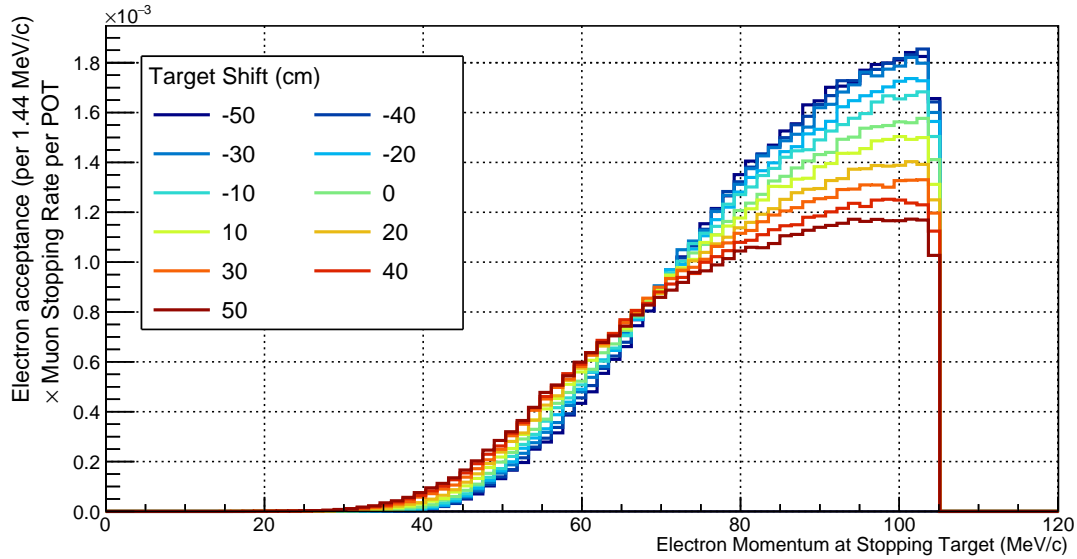


Figure 4.17: The momentum dependence of the electron acceptance into the detector for different target positions when the beam blocker is removed.

This correlation is also likely related to the way the acceptance changes for different target positions when the beam blocker is removed.

The second striking feature from the plots in Fig. 4.18 is the way the mean height acquires a strong sinusoidal component for large target shifts upstream. This suggests that when the target is shifted upstream the electrons passing the entrance to the spectrometer tend to have a particular value for the pitch and phase angles of the trajectories. Several separate mechanisms could produce this effect. Firstly the acceptance around the target itself could acquire a stronger preference for certain pitch and phase angles when the target is moved upstream. Secondly, since the stopping target disks will see more of the muon beam upstream, the muon stopping distribution could become less homogenous. Whilst electrons are produced isotropically path with less target material along them will tend to accept outgoing electrons more readily such that if more muons stop at one side of the target than the other a dependence on pitch and phase could arise.

Clearly then the stopping target region is a very complicated area; even though this study has focussed on a single parameter – the position of the target itself – it is clear that this correlates to many other variables. This is a region in the experiment most ripe for further optimisation then, and indeed appendix B shows some of the first steps that have made in this direction since the optimisation described here was completed. Unfortunately, at the time this work was carried out an error in the normalisation of these plots lead to the conclusion that the optimal shift was between 0 and 10 cm upstream.

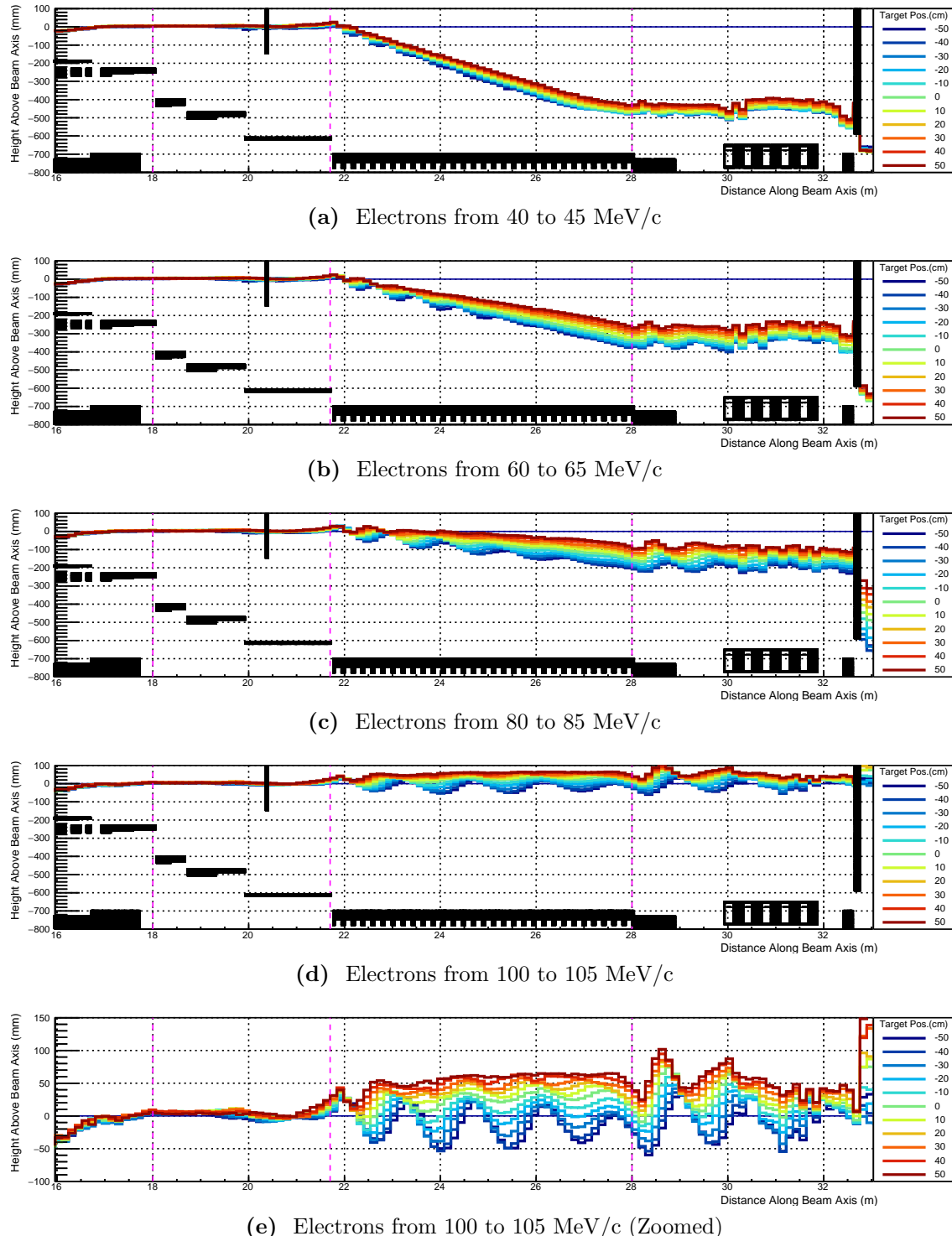


Figure 4.18: The effect of stopping target position on the height of electrons with a fixed momentum as they pass through the Electron Spectrometer. The size of the variation indicates the stability of the dipole tune; the two parameters are clearly correlated. Also striking – particularly in (e) – is the way the dependence on the helical pitch angles is affected by the stopping target position.

Given the complexity of the optimisation in this region, it was therefore decided to keep the stopping target at the nominal location for the subsequent steps. Having corrected the normalisation of the plots, the conclusion now is that the optimal location is between 10 and 20 cm upstream, so perhaps the target should have been shifted back. However the improvement to the sensitivity would have been small: shifting the target back about 20 cm improves the sensitivity by around 2% compared to the signal acceptance at nominal position.

4.6 Collimators in the Muon Beamline

With the beam line optimised for high signal efficiency, one can look at improving the background by adding collimators into the muon beam line to reduce the flux of high-momentum muons and pions.

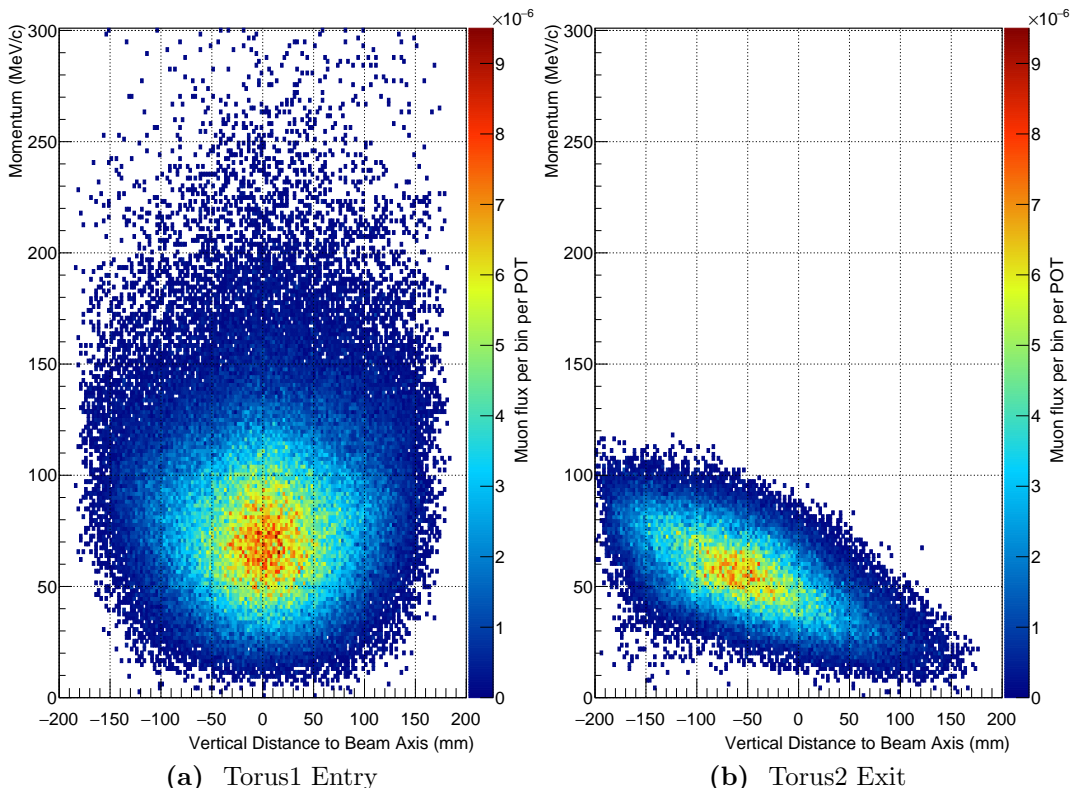


Figure 4.19: Dispersive effect of the 180° bent transport solenoid and dipole field on muons. No collimating material is yet included, so the high-energy muons being removed is due purely to the beam-pipe itself.

Fig. 4.19 shows the dispersive effect of the bent solenoid and dipole field on muons passing through the beamline. Thanks to this dispersion low momentum muons that can stop in the target and high momentum muons which could produce backgrounds are separated sufficiently so that material in the beam pipe can selectively remove the dangerous, high-momentum muons with only a small impact on the muon stopping rate.

4.6.1 Collimator Placement

The plots in Fig. 4.20 give a sense of where best to locate the collimating material. In Fig. 4.20a the paths of all muons along the beamline is shown. Fig. 4.20b then separates out the muons that stop in the target which should be compared to Fig. 4.20c showing the paths of muons that reach the stopping target region with momentum greater than 70 MeV/c (the threshold for a muon to decay to an electron with $p > 100$ MeV/c).

It is interesting to note the apparent asymmetry in the high-momentum muons at the entrance to the Torus1 that can be seen in Fig. 4.20c. This is not because of some momentum-dependence in the acceptance of the preceding beamline, but due to the fact that muons in that plot are only included if they are ‘dangerous’ in the region around the stopping target. Even without additional collimators, the beam pipe itself removes high momentum muons that enter in the lower half of the beamline. The validity of only tagging high momentum muons around the stopping target region comes from the assumption that the products of high-momentum muons that decay before this region can be reliably removed. It is important then that this assumption be checked, but for this work this is left as a task for the future.

Finally then in Fig. 4.20d the difference between the high-momentum muons and the paths of those that stop is shown. Regions in blue on this plot show where many more high-momentum muons pass than stopping muons; it is in these locations that collimator material will be most effective. This approach could also be improved, since taking the straight difference between the two plots implies equal weighting for stopping muons and high-momentum ones. In reality, whilst a muon tagged as stopping is definitely going to stop, a high-momentum muon should be weighted by the probability to produce a signal-like electron and the probability that this electron survives to be accepted into the detector, passing all analysis cuts. This would make the weighting for the high-momentum muons be a function of the beamline distance itself which again requires a study into how high-momentum electrons are accepted. However for the purposes of obtaining a qualitative sense of where to collimate the unweighted difference should be sufficient.

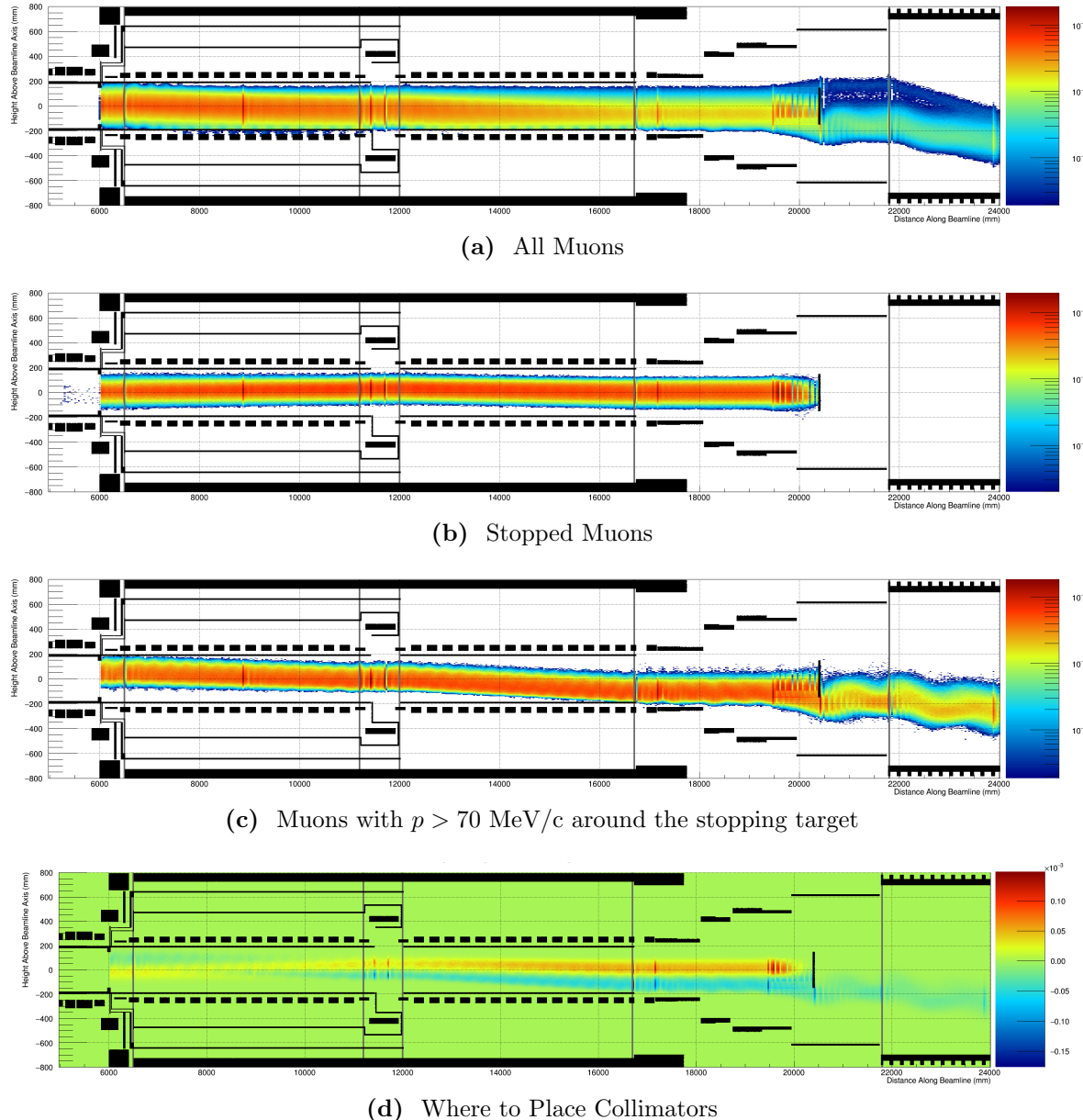


Figure 4.20: The heights of muons as they pass along the beamline. (a) The path of all muons. (b): The paths of muons that stop in the target. (c): The heights of muons with momentum greater than 70 MeV/c when they enter the region around the stopping target. These could potentially decay in flight to give electrons with 100 MeV/c or greater. (d): The difference between plot (b) and plot (c). Regions in dark blue would give the greatest impact in removing high momentum muons whilst leave the stopping muons untouched. These plots should be compared to those of Fig. 4.25 once collimators have been introduced.

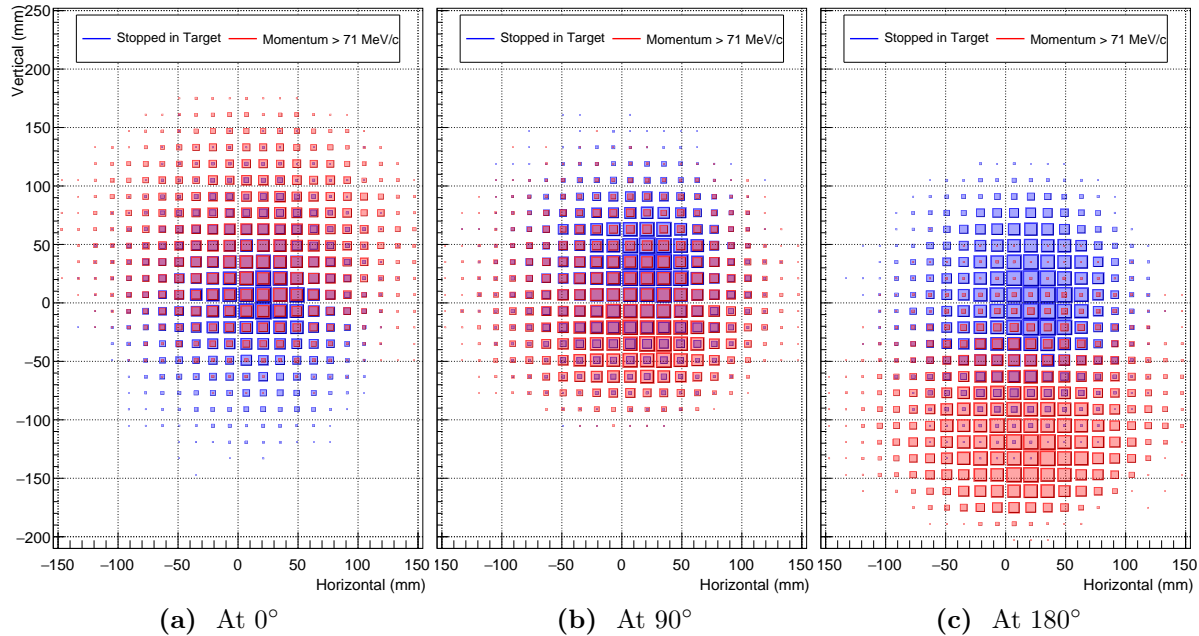


Figure 4.21: The separation between stopping and dangerous muons. The separation is largest at the exit (180°), reasonable at the entrance (0°), and smallest around the mid-point (90°).

Two regions of interest appear: in the upper half of the entrance to Torus1 and the lower half of the exit of Torus2. Collimating at the Torus1 entrance is justified by the basis that high momentum muons will tend to have larger gyroradii compared to the muons that stop, and that at this point the beam is largely on-axis and has not yet been dispersed. Collimating at the exit of Torus2 is readily understood on the grounds that the high momentum muons will have all drifted downwards by this point, compared to the low momentum stopping muons which are kept on-axis by the dipole fields.

These conclusions are backed by the plots shown in Fig. 4.21 which show transverse slices through the beamline at the entrance to Torus1 (0° of bent solenoid), the midpoint between Torus1 and Torus2 (after 90° of bent solenoid) and at the exit of Torus2 (after 180°). From these plots one can also see how in the middle of the bent solenoids (at 90°) the separation between muons that will stop and those that will have momentum greater than or equal to 70 MeV/c in the stopping target region is weakest, and hence collimators in this location will not be so effective.

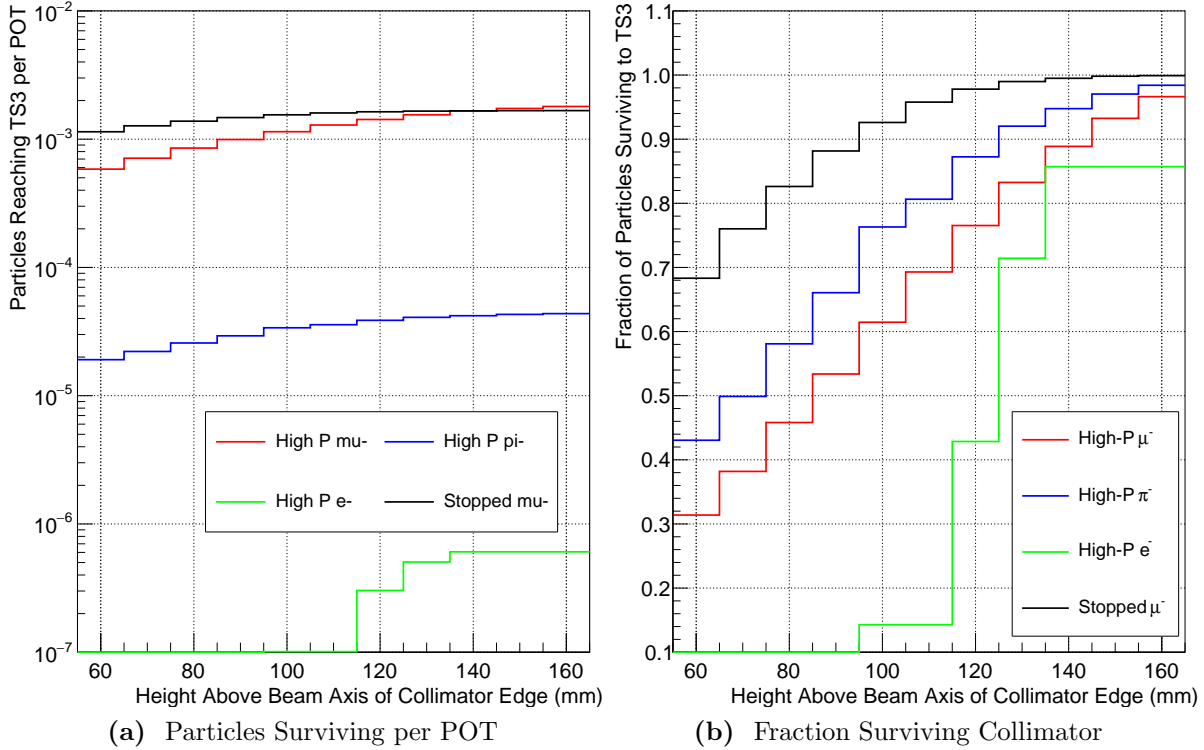


Figure 4.22: The effect of changing the height of the collimator in Torus1 on the particle distributions.

4.6.2 Collimator Height Optimisation

To identify the optimum height for the collimators in a computationally efficient way, events were generated without any collimators included. The full three dimensional trajectory of all particles as well as the decay tree were persisted. This allows for a ‘virtual’ collimator to be used, where particles that enter a defined region and their secondaries are removed from the downstream plots. Whilst this method allows for many collimator shapes and heights to be tested quickly, it comes with a couple of limitations. Firstly, the accuracy depends on the trajectory sampling density, which should be fine but this results in large data sizes. Secondly, realistic material effects of the collimator cannot be captured, such as the probability a particle is simply scattered rather than stopping completely, or the result of secondary particles produced in the collimator itself.

Fig. 4.22 shows the results of lowering the bottom edge of the collimator material in Torus1. Fig. 4.22a shows the probability per POT that different types of particle (stopped muons and high momentum muons, pions, and electrons) pass the collimator as a function of the collimator height. On the other hand, Fig. 4.22b shows the same plots

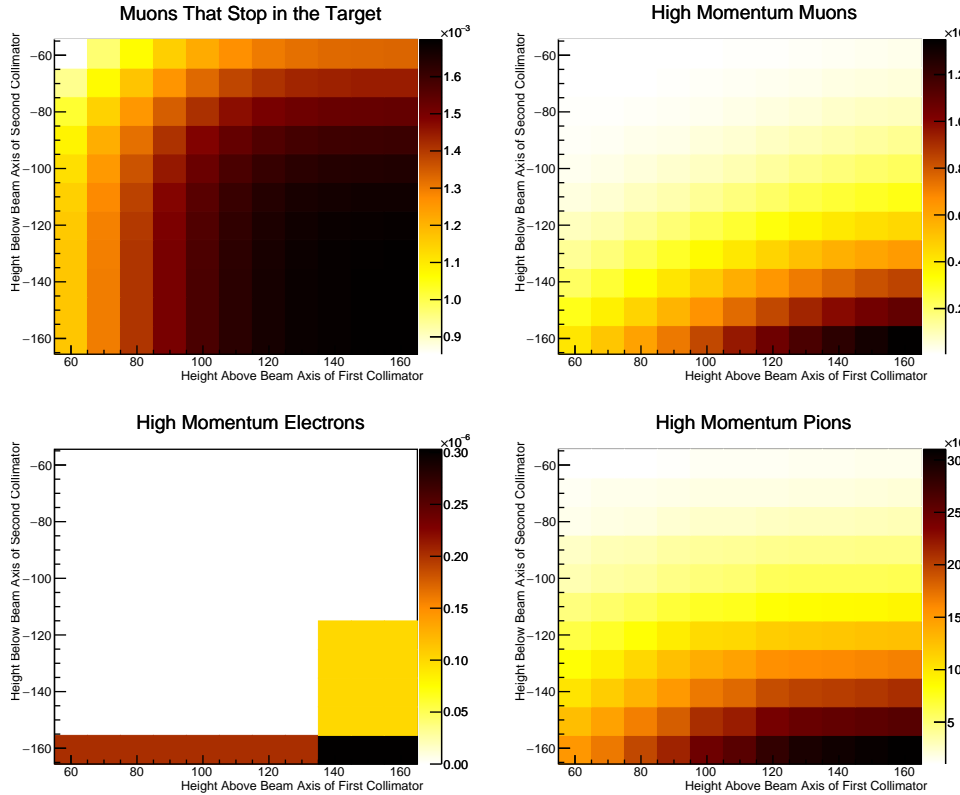


Figure 4.23: The number of particles reaching the end of the Torus2 solenoid relative to the number that enter the Torus1 solenoid (i.e. the survival probability) for different heights of both collimators in Torus1 and Torus2.

but normalised to the total number of each particle type that reaches the collimator in the first place, therefore showing the survival probability along just the collimator region. Based on these plots, for a collimator that starts at 120 mm above the beamline axis, 14% of high momentum pions are removed, high momentum muons are suppressed by 14% whilst the muon stopping rate is reduced only by 3%.

For the second collimator at the exit to Torus2, the situation is slightly more complicated since in principle the optimum height could be correlated to the height of the upstream Torus1 collimator. To account for this, the virtual collimator technique was applied for both the Torus1 and Torus2 collimator sections simultaneously. As a result, the 1-dimensional plots of Fig. 4.22 become 2D as can be seen in Fig. 4.23, which is normalised to the particle flux just before the collimator similar to Fig. 4.22b.

Fig. 4.24 represents the stopping and high-momentum plots in a way that is easier to compare the two directly. Each line in that plot is a contour showing a change of 2.5 percentage points to the yield. Total acceptance, or 100% is in the bottom right

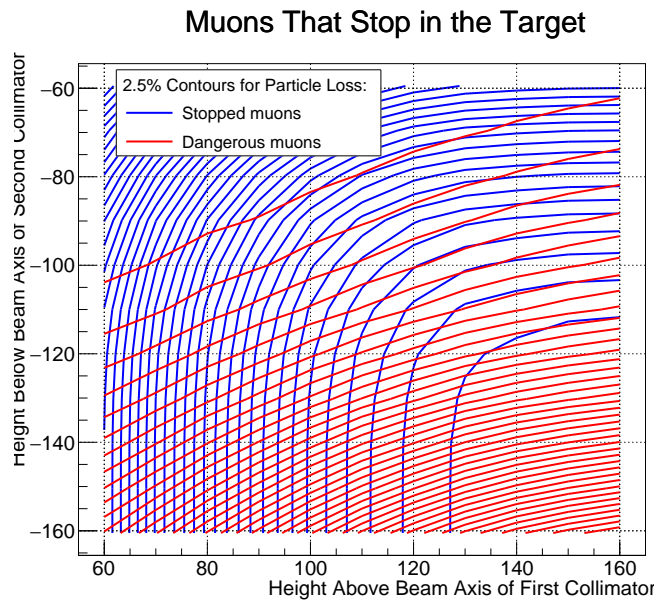


Figure 4.24: 2.5% contours showing how changing the collimator height affects the stopped and high-momentum muon rates. Each contour represents a reduction of 2.5 percentage points to the particle flux, with 100% acceptance sitting in the bottom right. Blue lines represent the flux of stopping muons, whilst red lines represent the flux of high-momentum muons. For example, for collimator heights within the first blue contour towards the bottom-right corner, less than 2.5% of stopped muons are lost.

corner. From this plot it can be seen that whilst keeping more than 97.5% of the muon stopping rate (the bottom-right most blue contour), the maximum high momentum muon suppression is achieved when the Torus1 collimator sits about 140 mm above the beam axis, and the Torus2 collimator sits about 120 mm below it. To be precise, at these collimator values the muon stopping rate is kept at 99% of the no-collimator rate, whilst high momentum pions, muons and electrons drop to 27.6%, 20.9% and 11% (although this last value is very statistically limited) respectively, compared to their no-collimator rates. At this point the selected values for the collimator heights give conservative background suppressions and tighter values could be chosen. Given that backgrounds from high-momentum muons are suppressed compared to the actual rate of 'dangerous' muons by the geometric acceptance of the remaining beamlne and the timing and momentum cuts this seems reasonable at this stage although this will of course be investigated in the next chapter.

Finally, for comparison to the original plots, Fig. 4.25 shows the impact the new collimators have on the muon components of the beam. It is clear how greatly reduced the number of muons passing the stopping target region has now become.

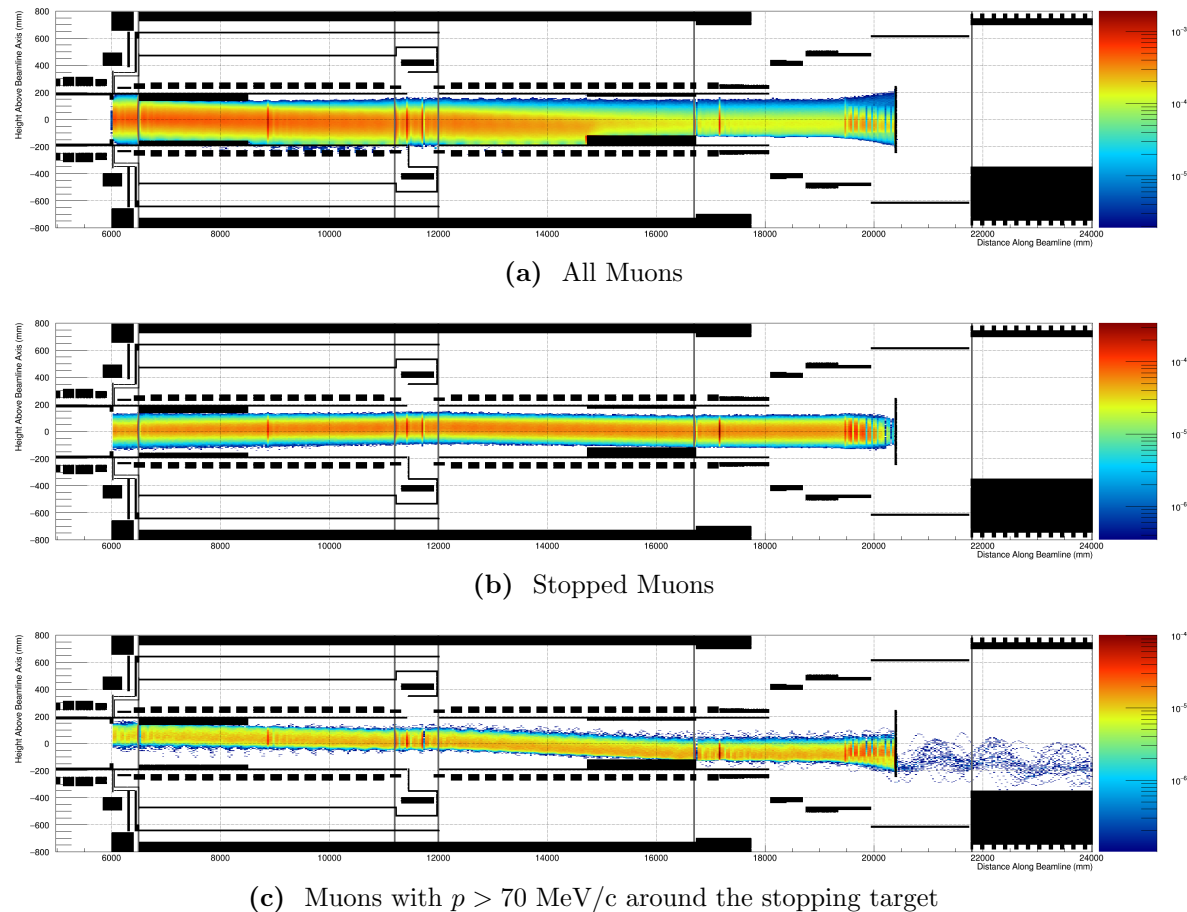


Figure 4.25: The heights of muons as they pass along the beamline. (a) The path of all muons. (b): The paths of muons that stop in the target. (c): The heights of muons with momentum greater than 70 MeV/c when they enter the region around the stopping target. These could potentially decay in flight to give electrons with 100 MeV/c or greater. These plots should be compared to those of Fig. 4.20 before collimators were introduced, where it is clear how well the dangerous muons are being suppressed.

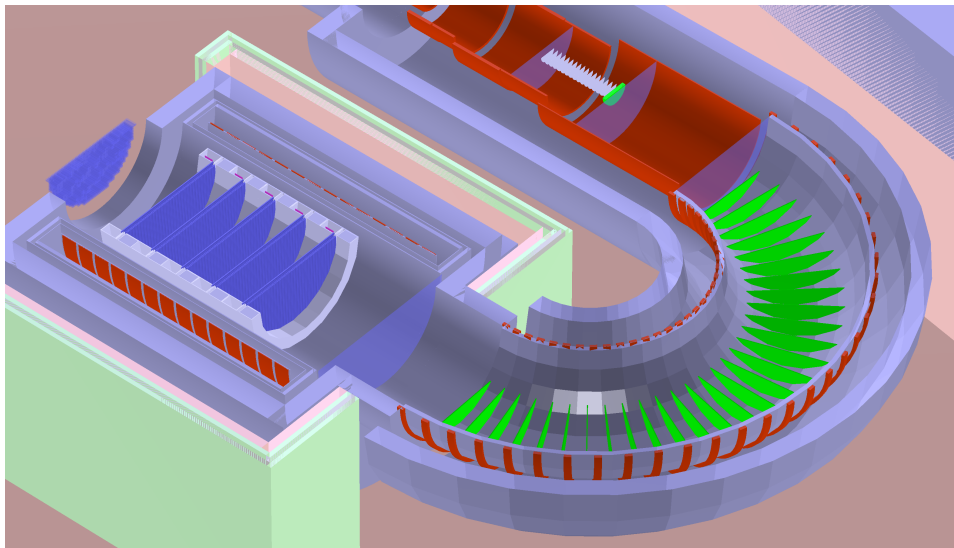


Figure 4.26: Location of the beam blocker and one possible geometry for the DIO blockers, both highlighted in green, shown here before optimisation.

4.7 The Beam and Decay-in-Orbit Blockers

For every muonic atom formed in the stopping target some 39% will undergo decay in orbit (DIO). With some 1.4×10^8 POT per bunch and a muon stopping efficiency around 1.7×10^{-3} stops per POT, one can expect about 9×10^4 DIO events per bunch. If the detector system were exposed to this level of hits it would be impossible to resolve any signal electrons. However, above the end-point energy for electrons coming from free muon decay, the DIO spectrum falls extremely quickly, with around 99% of DIO electrons being produced with less than 60 MeV/c (*((CHECK: Are these the exact numbers, is my memory correct?))*). To this end the electron spectrometer's primary purpose is to disperse away the electrons below 60 MeV/c whilst keep signal electrons on-axis, such that material in the beamline can be tuned to remove the low energy DIO electrons. The beam and DIO blockers are highlighted in green in Fig. 4.26.

Fig. 4.27 demonstrates the dispersion that appears at the end of the spectrometer with the nominal beam blocker design and no DIO blockers in place. The DIO blockers will be inserted along the bottom of the spectrometer and tuned to scrape away a sufficient number of DIO electrons, which will tend to travel towards the bottom of the beam pipe. However whilst the centre of gyration drifts with a well-behaved proportionality in a bent solenoid, the actual separation between signal and DIO electrons is in reality less clear as can be seen by the lower plot in Fig. 4.27.

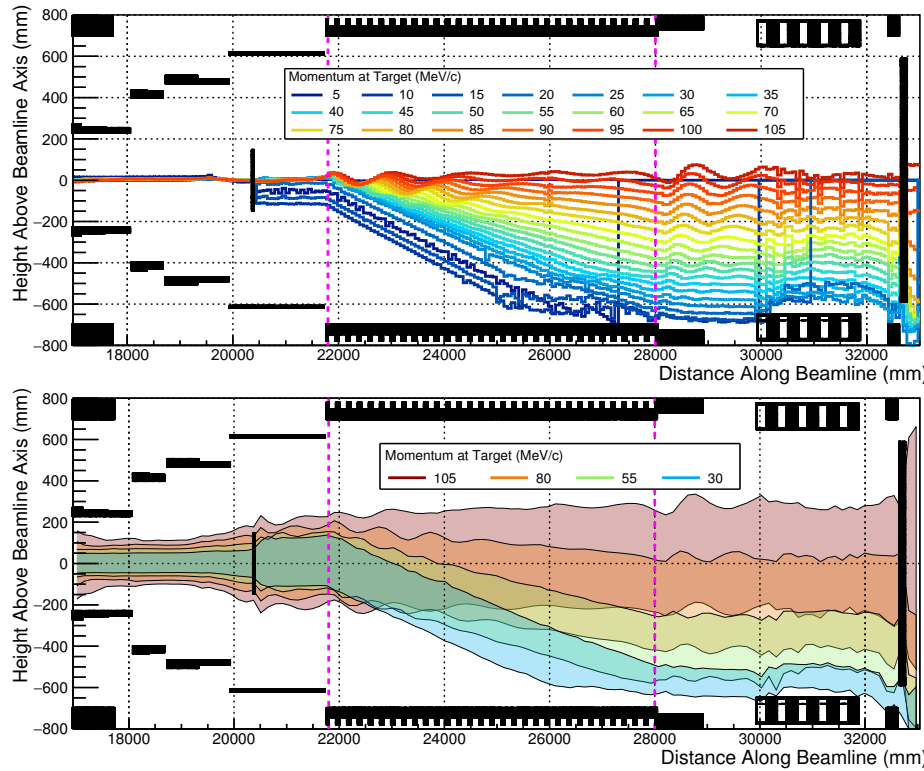


Figure 4.27: Momentum-dependent dispersion of electrons passing through the spectrometer. Top plot: the mean height of different momenta electrons as a function beamline distance, showing how the drift of the centre of gyration is truly proportional to the momentum. Bottom plot: single standard deviation bands for electrons at different momentum, which shows how the envelope for different momenta overlap considerably, reducing the effectiveness of any collimators.

In addition to the DIO blockers along the spectrometer, the material of the beam blocker immediately after the stopping target also plays a role in suppressing the **DIO** rate since low energy electrons remain closer to the beam axis, as can be seen in the lower plot of Fig. 4.27 around the stopping target.

This section therefore describes a simultaneous optimisation of the beam blocker radius and the DIO blocker height. The overall goal is to suppress the DIO rate to less than a single DIO electron per bunch whilst maintain maximal signal acceptance. As for the muon beam collimators, we use the analysis-based collimator approach, where no blocking material is included during simulation. Instead a high-sampling density for particle trajectories is used such that during analysis particles and their secondaries can be ‘killed’ if they enter a region that would contain material of either the DIO or beam blocker.

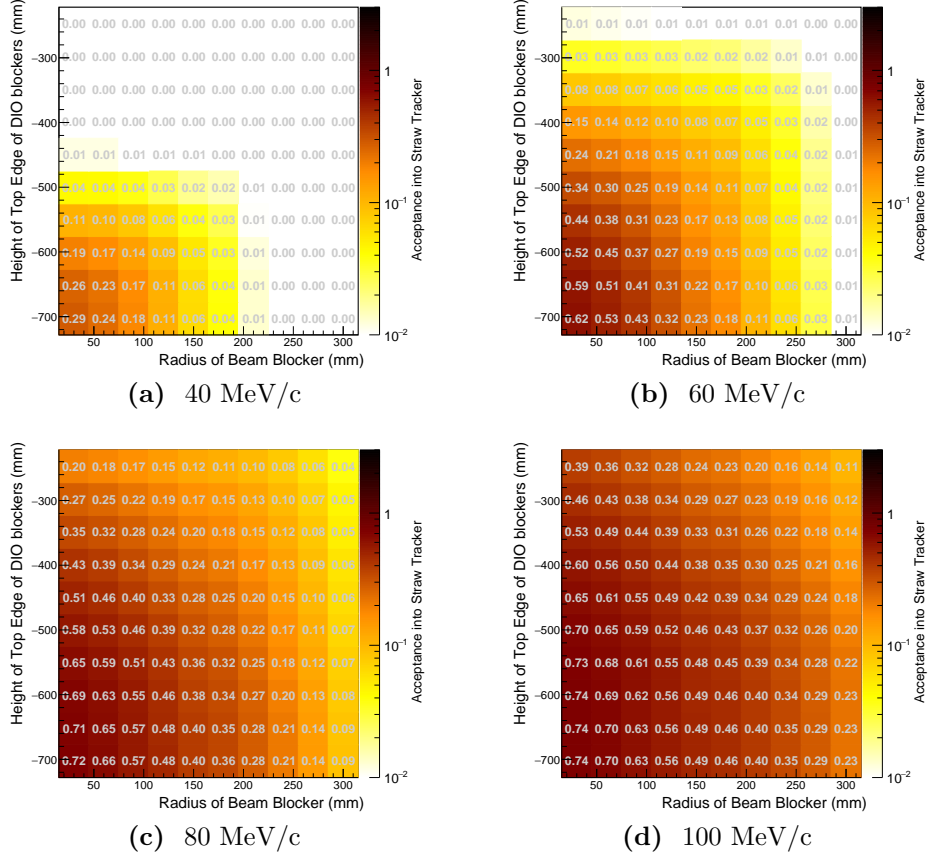


Figure 4.28: Acceptance into the straw tracker for electrons with different momentum at the stopping target as a function of the beam and DIO blocker dimensions. Note the logarithmic scale for the colour bar.

The results of this study are shown in Fig. 4.28, where the geometric acceptance into the detector is shown for four different electron momenta as a function of the beam blocker radius and DIO blocker height. It is clear that for all values of the blockers' dimensions, electrons above 100 MeV/c have a much better acceptance.

The mean hit rate per DIO event is shown in Fig. 4.29a. It is formed by, for each combination of DIO and beam blocker dimension, the weighted integral of the acceptance of electrons as a function of momentum with the mean DIO rate in each momentum bin. To compare the hit rate to the acceptance of signal, the ratio between the hit rate and the high-momentum electron acceptance is shown in Fig. 4.29b. It is clear from this figure how quickly (note the logarithmic colour scale) the DIO hit rate is suppressed by increasing the DIO and beam blocker dimensions compared to the signal acceptance.

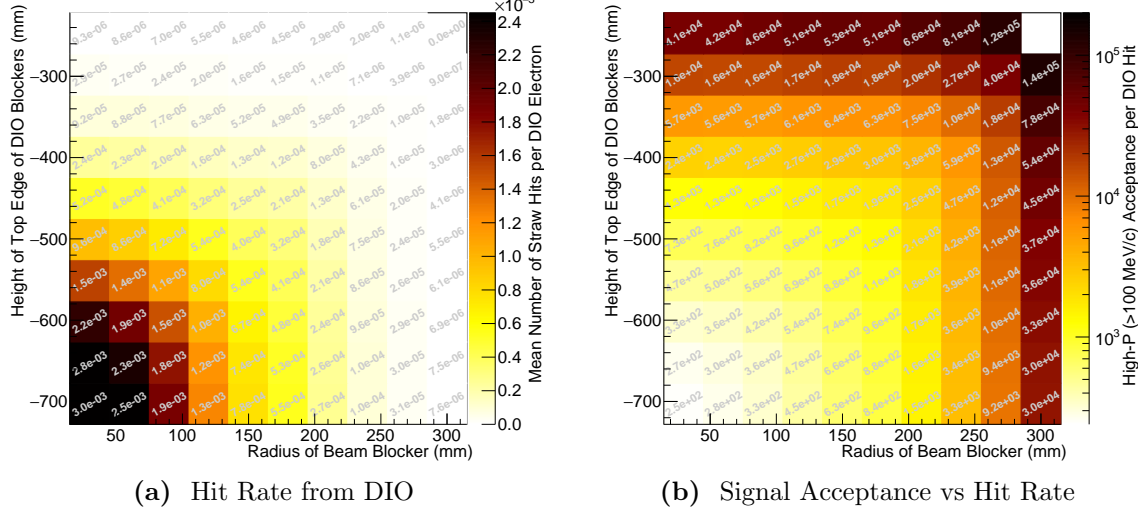


Figure 4.29: (a) Number of straw tracker hits per DIO electron. (b) Ratio between the high-momentum electron ($p > 100 \text{ MeV}/c$) acceptance to the number of hits per DIO electron. Colour is on a logarithmic scale.

With a beam blocker of 24 cm radius and DIO blockers set to 35 cm below the beam axis, the DIO hit rate is about 2.2×10^{-5} per DIO event, or about 2 DIO hits per bunch. For the same blocker dimensions, the geometric signal acceptance is about 0.22%. Given the steep drop-off in hit rate versus signal acceptance around these values a finer scan in this region is an important check for the future. What hit rate in the straw tracker is tolerable is a number for future studies. In Phase-I, the straw tracker is expected to operate with a hit rate around 1 kHz per straw. Phase-II will likely use finer straws, but with the current Phase-I design, some 133 straws occupy a layer, so that a total hit rate into the Straw Tracker of around 200 kHz should be acceptable.

Given the scope for future improvements in the granularity of the Phase-II straw tracker and the sensitivity to the beam and DIO blocker dimensions, the somewhat non-conservative values described above of 24 cm and 35 cm for beam blocker radius and DIO blocker depth below the beam axis are selected here.

4.8 Summary of optimised parameters

The complete set of optimised parameters is shown in Table 4.4.

Parameter	Value	Comments
Production Target Length	32 cm	Placed asymmetrically about muon beamline axis
Production Target Radius	1 cm	
Torus1 (TS2) Dipole Strength	0.055 T	same as Phase-I
Torus2 (TS4) Dipole Strength	0.0275 T	same as Phase-I
Torus1 Entrance Collimator Height	14 cm above beam axis	From top of beam pipe downwards
Torus2 Exit Collimator Height	12 cm below beam axis	From bottom of beam pipe upwards
Stopping Target Location	0 cm	Unchanged from CDR value
Electron Spectrometer Dipole	-0.18 T	Negative compared to Torus1 and Torus2 dipole fields
Beam Blocker Radius	24 cm	
DIO Blocker Height	35 cm below beam axis	From bottom of spectrometer upwards

Table 4.4: Optimised values for the parameters studied in this chapter. Many more parameters remain to be optimised that were considered beyond the scope of the present work.

4.9 Future optimisations

The primary goal of this work is to update the previous optimisation from the 2009 CDR and provide a new baseline design. However whilst touching every aspect of the layout of Phase-II, the optimisation developed here is not exhaustive and there is much scope for further work.

The following list is a short summary of some of the areas that could be developed further:

Refine the optimisation criteria In many of these studies only the signal efficiency, or even some proxy, is used to identify the optimal value of the parameter under question. In reality one ought also to study simultaneously the background rates. These two quantities should be combined into the expected confidence limits given a null or background-only measurement. At the same time other quantities such as cost and run-time will also need considering, although the latter is likely reduced simultaneously with maximising the overall sensitivity.

High energy electron acceptance vs beamline distance When tuning the muon beam collimators, the key goal is to remove high-energy particles that can produce high energy electrons. A particularly useful study would be to evaluate the acceptance to signal-like electrons which originate along the beamline. This should include those electrons which originate with momentum greater than 105 MeV/c but which arrive at the detector with signal-like energies. With this information, it becomes easier to identify how soon along the beamline one must collimate away the high-energy particles which may lead to improvements in the muon stopping rate or the signal acceptance.

Stopping target shape, thickness, disk spacing etc This study has focussed only on the position of the stopping target. Clearly the actual shape should be studied as well. In particular, given the dispersion in the muon beam, and the changing solenoidal field strength around the target, a target design that uses disks of varying profile or even thickness has potential to improve the experimental sensitivity.

Correlation between dipole fields and stopping target shape Since the bent solenoids introduce dispersion into the beam and the dipole fields compensate for this, the height and momentum of the muon beam at the stopping target can be controlled to a degree. Whilst in the optimisation of the muon beam dipoles of this thesis the target shape was held fixed, in principle some of the identified correlations might be different if the target design was allowed to vary simultaneously. Such a study would clearly involve an enormous parameter space, so perhaps this is a study that could be best performed with a smarter machine-learning based approach.

Spectrometer's solenoidal field strength and aperture Since the dispersive effect of a bent solenoid is inversely proportional to the solenoidal field strength, reducing the field in the spectrometer will likely improve the DIO–signal separation, reducing the hit rate. This could however also affect the signal acceptance since the trajectories will acquire larger envelopes. Increasing the spectrometer aperture size could compensate this, but then one faces an increase in the cost of the spectrometer and the detector solenoid which would need to be considered.

Chapter 5

Phase-II Signal Sensitivity

List of Acronyms

CDC Cylindrical Drift Chamber

CDR Conceptual Design Report

CERN Organisation européenne pour la recherche nucléaire

CyDet Cylindrical Detector

DIO decay in orbit

JFY Japanese Fiscal Year

J-PARC the Japanese Proton Accelerator Research Complex

LYSO Cerium-doped Lutetium Yttrium Oxyorthosilicate

MR J-PARC Main Ring

PID Particle Identification

POT Protons on Target

RCS J-PARC Rapid Cycling Synchrotron

SES Single-Event Sensitivity

SM Standard Model

StrECAL Straw tube tracker and Electromagnetic Calorimeter

TDR Technical Design Report

Bibliography

- [1] see: <http://ilcsoft.desy.de/marlin>.
- [2] see: <http://www.cmtsite.org>. No longer maintained.
- [3] see: <http://www.cmake.org>.
- [4]
- [5] MIDAS (Maximum Integration Data Acquisition System). <http://midas.psi.ch>. Accessed: 22-May-2015.
- [6] K. Abe, N. Abgrall, H. Aihara, Y. Ajima, J.B. Albert, and D. Allan. The t2k experiment. *Nuclear Instruments and Methods in Physics Research Section A: Accelerators, Spectrometers, Detectors and Associated Equipment*, 659(1):106 – 135, 2011.
- [7] S. Agostinelli, J. Allison, K. Amako, J. Apostolakis, H. Araujo, P. Arce, M. Asai, D. Axen, S. Banerjee, G. Barrand, F. Behner, L. Bellagamba, J. Boudreau, L. Broglia, A. Brunengo, H. Burkhardt, S. Chauvie, J. Chuma, R. Chytracek, G. Cooperman, G. Cosmo, P. Degtyarenko, A. Dell'Acqua, G. Depaola, D. Dietrich, R. Enami, A. Feliciello, C. Ferguson, H. Fesefeldt, G. Folger, F. Foppiano, A. Forti, S. Garelli, S. Giani, R. Giannitrapani, D. Gibin, J.J. Gmez Cadenas, I. Gonzlez, G. Gracia Abril, G. Greeniaus, W. Greiner, V. Grichine, A. Grossheim, S. Guatelli, P. Gumlplinger, R. Hamatsu, K. Hashimoto, H. Hasui, A. Heikkinen, A. Howard, V. Ivanchenko, A. Johnson, F.W. Jones, J. Kallenbach, N. Kanaya, M. Kawabata, Y. Kawabata, M. Kawaguti, S. Kelner, P. Kent, A. Kimura, T. Kodama, R. Kokoulin, M. Kossov, H. Kurashige, E. Lamanna, T. Lampn, V. Lara, V. Lefebure, F. Lei, M. Liendl, W. Lockman, F. Longo, S. Magni, M. Maire, E. Medernach, K. Minamimoto, P. Mora de Freitas, Y. Morita, K. Murakami, M. Nagamatu, R. Nartallo, P. Nieminen, T. Nishimura, K. Ohtsubo, M. Okamura, S. O'Neale, Y. Oohata, K. Paech, J. Perl, A. Pfeiffer, M.G. Pia, F. Ranjard, A. Rybin, S. Sadilov, E. Di Salvo, G. Santin, T. Sasaki, N. Savvas, Y. Sawada, S. Scherer, S. Sei, V. Sirotenko, D. Smith, N. Starkov, H. Stoecker, J. Sulkimo, M. Takahata, S. Tanaka, E. Tcherniaev, E. Safai Tehrani, M. Tropeano, P. Truscott, H. Uno, L. Urban, P. Urban, M. Verderi, A. Walkden, W. Wander, H. Weber, J.P. Wellisch, T. Wenaus, D.C. Williams, D. Wright, T. Yamada, H. Yoshida, and D. Zschiesche. Geant4 - a simulation toolkit. *NIM in PRS A*, 506(3):250 – 303, 2003.
- [8] AlCap Collaboration. Study of muon capture for muon to electron conversion ex-

- eriments. http://muon.npl.washington.edu/exp/AlCap/R-13-03.1_BV44.pdf. Accessed: 28-October-2015.
- [9] D. Armutliiski, Ts. Baatar, Ts. Batsaikhan, T. Kanarek, E.N. Kladnitskaya, M.U. Sultanov, R. Togoo, G.P. Toneeva, and D. Tuvdendorzh. Hadron spectra in hadron - nucleus collisions. 1991.
 - [10] G. Barrand, I. Belyaev, P. Binko, M. Cattaneo, R. Chytracek, et al. GAUDI - A Software Architecture and Framework for Building HEP Data Processing Applications. *Comput.Phys.Commun.*, 140:45–55, 2001.
 - [11] Wilhelm H. Bertl et al. A Search for muon to electron conversion in muonic gold. *Eur.Phys.J.*, C47:337–346, 2006.
 - [12] S. V. Boyarinov, I. I. Evseev, Yu. T. Kiselev, G. A. Leksin, A. N. Martemyanov, K. R. Mikhailov, S. A. Pozdnyakov, Yu. V. Terekhov, V. I. Ushakov, and V. A. Sheinkman. Yields of p, anti-p, pi+-, and K+- emitted at an angle of 97-degrees in the laboratory system from nuclei irradiated by 10.14-GeV protons. *Phys. Atom. Nucl.*, 57:1379–1388, 1994. [Yad. Fiz.57,1452(1994)].
 - [13] M. G. Catanesi et al. The HARP detector at the CERN PS. *Nucl. Instrum. Meth.*, A571:527–561, 2007.
 - [14] COMET Collaboration. Conceptual design report for experimental search for lepton violating $\mu^- e^-$ conversion at sensitivity of 10^{-16} with a slow-extracted bunched proton beam (COMET), J-PARC P21.
 - [15] Comet group on Gitlab. <https://gitlab.in2p3.fr/comet>.
 - [16] Andrzej Czarnecki, Xavier Garcia i Tormo, and William J. Marciano. Muon decay in orbit: Spectrum of high-energy electrons. *Phys.Rev.*, D84(1):013006, 2011.
 - [17] Rashid M. Djilkibaev. Meco muon yield simulation using experimental data. Technical report, Department of Physics and Astronomy, University of California.
 - [18] Andrew Williams John Edmonds. *An Estimate of the Hadron Production Uncertainty and a Measurement of the Rate of Proton Emission after Nuclear Muon Capture for the COMET Experiment*. PhD thesis, U. Coll. London, 2015.
 - [19] Alfredo Ferrari, Paola R. Sala, Alberto Fasso, and Johannes Ranft. FLUKA: A multi-particle transport code (Program version 2005). 2005.
 - [20] G4Beamline. G4beamline homepage. 2009. <http://www.muonsinternal.com/muons3/G4beamline>.
 - [21] C. Hoppner, S. Neubert, B. Ketzer, and S. Paul. A Novel Generic Framework for Track Fitting in Complex Detector Systems. *Nucl. Instrum. Meth.*, A620:518–525, 2010.
 - [22] H. Iwase, K. Niita, and T. Nakamura. Development of general-purpose particle and

- heavy ion transport monte carlo code. *Journal of Nuclear Science and Technology*, 39(11):1142–1151, 2002.
- [23] Yu. T. Kiselev, V. A. Sheinkman, A. V. Akindinov, M. M. Chumakov, A. N. Martemyanov, V. A. Smirnitsky, Yu. V. Terekhov, and E. Ya. Paryev. Probing of compact baryonic configurations in nuclei in $A(p, \bar{p})X$ reactions and antiproton formation length in nuclear matter. *Phys. Rev.*, C85:054904, 2012.
 - [24] Ben Krikler, Ajit Kurup, Yoshi Uchida, Andrew Edmonds, Phill Litchfield, and the COMET Collaboration Software Group. Icedust conventions. *Internal Document*.
 - [25] Robert K Kutschke. art: A framework for new, small experiments at fermilab. *Journal of Physics: Conference Series*, 331(3):032019, 2011.
 - [26] Nikolai V. Mokhov. The MARS code system user’s guide version 13(95). 1995.
 - [27] T. Suzuki, D. F. Measday, and J. P. Roalsvig. Total nuclear capture rates for negative muons. *Phys. Rev. C*, 35:2212–2224, Jun 1987.
 - [28] The COMET Collaboration. COMET Phase-I: Technical Design Report. Technical report, KEK, April 2016.
 - [29] Nam Hoai Tran. A Study of Proton Emission Following Nuclear Muon Capture for the COMET Experiment. *Thesis*, 2014.
 - [30] D. H. Wright and M. H. Kelsey. The Geant4 Bertini Cascade. *Nucl. Instrum. Meth.*, A804:175–188, 2015.